

Laser-Assisted Focused-Ion-Beam-Induced Deposition of Copper

by

Jun Funatsu

B. Eng., Mechanical Engineering,
Tokyo Institute of Technology (1987)

Submitted to the Department of Materials Science and Engineering in
Partial Fulfillment of the Requirements for the Degree of

Master of Science
in Materials Science and Engineering

at the

Massachusetts Institute of Technology

May 1994

© 1994 Massachusetts Institute of Technology
All rights reserved

Signature of Author
Department of Materials Science and Engineering
May 6, 1994

Certified by
Carl V. Thompson II
Professor of Electronic Materials
Thesis Advisor

Accepted by
Carl V. Thompson II
Professor of Electronic Materials
Chair, Departmental Committee on Graduate Students

MASSACHUSETTS INSTITUTE
OF TECHNOLOGY

Laser-Assisted Focused-Ion-Beam-Induced Deposition of Copper

by

Jun Funatsu

Submitted to the Department of Materials Science and Engineering
on May 6, 1994

in partial fulfillment of the requirements for the degree of
Master of Science
in Materials Science and Engineering

Abstract

As the minimum feature size becomes on the order of submicron dimensions, techniques to directly repair VLSI circuits and x-ray masks, techniques for so-called "microsurgery", are increasingly important. Focused ion beam (FIB) techniques have been commercially used to deposit conductors and insulators and remove materials in a localized area on substrates. Copper, which is a candidate future conductor material in VLSI circuits due to its low resistivity and high electromigration resistance, has been deposited from the organometallic complex, Cu(hfac)TMVS, using 25 keV gallium ions from liquid ion source. Earlier work has shown that substrate heating can lead to FIB-induced deposition of high conductivity Cu lines. In this work, use of a laser for localized heating for FIB-induced deposition has been investigated as an alternative to heating of the entire substrate. For laser-assisted FIB-induced deposition, a "high power" semiconductor laser, of wavelength 977 nm and output power ranging continuously from 0 to 1.2 W, was used. The laser was focused onto a thermally oxidized Si substrate, and its spot area is estimated to be $5.90 \times 10^{-5} \text{ cm}^2$, which gives the maximum intensity of $2.0 \times 10^4 \text{ W/cm}^2$. Cu(hfac)TMVS has no absorption in the gas phase at 977 nm. As a result, for films deposited using this laser, the dependencies of the growth rate and resistivity on the estimated substrate temperature are in good agreement with those of films deposited using conventional resistance heating. The growth rate ranges from 2.0 to 4.3 Å/s, depending on the laser power. A small decline in the growth rate in the relatively low laser power regime was observed. At higher laser powers, the growth rate is significantly increased. The lowest resistivity lines, $3 \mu\Omega\text{-cm}$ (close to the resistivity of bulk copper, $1.7 \mu\Omega\text{-cm}$), has been achieved when deposited at 1.1 W of laser power. At this laser power, the substrate temperature is estimated to be 120 °C. The smallest line width, 0.8 μm , has been achieved when deposited without using the laser. The deposited lines become slightly wider for higher laser powers, causing the aspect ratio to be smaller. When deposited at high temperature, the deposited film becomes coarse and granular. Laser-assisted, FIB-induced deposition has been demonstrated as a means of writing high conductivity submicron Cu lines.

Thesis Advisor: Carl V. Thompson II

Title: Professor of Electronic Materials

Acknowledgments

I would like to take this opportunity to thank those who have given me the support to carry out this research. I am particularly grateful to my advisor at MIT, Prof. Carl V. Thompson, and former advisor, Dr. John Melngailis, for their invaluable advice and support. I would like to thank Dr. James N. Walpole and Leo J. Missaggia at Lincoln Laboratories, MIT, for their technical support, and loaning a state-of-the-art semiconductor laser and setting up the optical system. I am thankful to Leonard I. Sudenfield of the Electron Microscopy Facility, Timothy McClure of the Microelectronics Technologies Facility, and Franklin Payne and Nagel Stone of the Machining Facilities at the Center for Materials Science and Engineering for their kind and patient assistance. I learned much from Anthony Della Ratta about FIB operation and other experimental procedures. I am also grateful to Brett Knowlton and Young-Chang Joo for their technical assistance in electrical measurements and optical microscopy. I am most grateful to Tony Chiang and Frank Ross for their technical assistance in FIB and critique of my thesis. Finally, I most acknowledge the love and support of my wife, Tomomi. Without her understanding and generosity, not only my thesis but also entire study at MIT would have been impossible to accomplish.

Thank you, Kim-chan.

Contents

List of Figures	6
1 Introduction	10
1-1 Photolithography	10
1-2 Focused Ion Beam System	14
1-3 Focused Ion Beam Application	19
1-4 Objectives	26
2 Experiments	27
2-1 Focused Ion Beam System	27
2-2 Semiconductor Laser and Optics	30
2-3 Copper Precursor	35
2-4 Scanning Electron Microscopy	37
2-5 Deposition	38
2-6 Yield and Growth Rate Measurement	40
2-7 Resistivity Measurement	40
2-8 Summary	42
3 Results and Discussion	43
3-1 Substrate Temperature	43
3-2 Yield and Growth Rate	45
3-3 Resistivity	47
3-4 Microstructure	52
3-5 Summary	56
4 Summary and Future Work	57
4-1 Summary	57
4-2 Future Work	58

Appendix A:

Temperature Calculation	59
A-1 Infinite Sheet Model	59
A-2 Heat Transfer Model	62

Appendix B:

Total Efficiency in Laser Beam Irradiation	65
B-1 General Theory of Optics	66
B-2 Calculation of the Net Efficiency	70

Bibliography	73
---------------------------	----

List of Figures

1-1	(a) Increase in the number of transistors per microprocessor chip versus year of introduction, for a variety of 8-bit and 16-bit microprocessors, and (b) the decrease in minimum device feature size versus time on integrated circuits [1].	11
1-2	Exposure and development of negative and positive photoresists, and resulting etched film patterns [1].	12
1-3	Three basic ion sources and their characteristics [4].	15
1-4	Schematic diagram of focused ion beam optics [5].	17
1-5	Plot of natural log of the current versus distance from the center of the beam [13]. The squares are measured data, the center curve is the Gaussian fit (FWHM = 0.5 μm) and the lines are fits to the exponential tails.	18
1-6	Schematic diagram of (a) ion beam milling, (b) lithography, (c) maskless ion implantation, and (d) ion beam induced deposition	21
1-7	Schematic of (a) the binary collision model and (b) the thermal spike model[19].	23
2-1	The FIB system, FEI 500D, block diagram[33].	28
2-2	A schematic of the specimen chamber.	29
2-3	Junction-side-up view of the semiconductor laser with tapered contact region and etched grooves to spoil the cavity[34].	30
2-4	The output power measured at the output window with an anti-reflection coating. Shown as a function of the diode current for the InGaAs/AlGaAs heterostructure laser at room temperature.	31
2-5	Schematic representation of far-field emission of a stripe-geometry double-heterostructure laser[37].	31

2-6	Experimental se-up to measure the far field pattern of a semiconductor laser.	33
2-7	The far field intensity profile of the output beam along the slow axis. The Gaussian function was fit to the data.	33
2-8	Copper (I) hexafluoro-acetyl acetone trimethyl-vinyl-silane.	35
2-9	Clausius-Clapeyron vapor pressure/temperature plot of Cu(hfac)TMVS.	36
2-10	Block diagram of an electron optical column of an SEM[1].	37
2-11	Finger pattern used for four point probe measurements.	41
3-1	Temperature rise during the laser irradiation. Unfilled squares, diamonds, circles, and triangles are temperatures measured with a thermocouple when the laser output powers are 1.07, 0.948, 0.63, and 0.28 W, respectively. Each line is the calculated temperature at the corresponding output power.	44
3-2	Dimensionless temperature as a function of temperature. The dashed line was fit to the measured values.	45
3-3	Yield and growth rate as a function of laser power. The yield was calculated assuming a rectangular cross-section, and using the bulk copper density.	46
3-4	Schematic of focused-ion-beam-induced decomposition process of Cu(hfac)TMVS.	47
3-5	Resistivity as a function of laser power. The smallest resistivity of 3 $\mu\Omega$ -cm has been achieved at laser power of 1.15 W.	48
3-6	Resistivity as a function of estimated substrate temperature. The results from the previous study by Della Ratta are also shown for comparison[19]. In the previous study, the substrate was heated by a resistance-heated substrate holder, and the films were deposited at a local precursor pressure at 1.5 mtorr at an average ion current density of 20 $\mu\text{A}/\text{cm}^2$ using 35 keV Ga ions.	49

3-7	The resistance of deposited lines as a function of inverse deposition time. The laser power used was 1.12 W, and the substrate temperature was estimated to be 120 °C. The line width and length are 1.6 and 100 μm , respectively. The dashed line indicates the resistance calculated by taking bulk copper resistivity and a constant growth rate of 4.3 $\text{\AA}/\text{s}$	51
3-8	The normalized resistivity as a function of deposition time. The resistivity is obtained by using a constant growth rate of 4.3 $\text{\AA}/\text{s}$	51
3-9	Scanning electron micrographs of copper lines deposited for (a) 1 minute and (b) 10 minutes without laser irradiation.	53
3-10	A scanning electron micrograph of a copper line deposited for 10 minute with laser irradiation of 1 W. The substrate temperature is estimated to be 110 °C.	54
3-11	The line width and aspect ratio of the deposited copper lines as a function of laser output power. The aspect ratio is obtained by dividing the line height by line width.	55
A-1	Schematic of the infinite sheet model with a cylindrical heat source. The total power P is focused to a circular area (πw_0^2) on the surface. w_0 is the beam diameter and I_0 is the average beam intensity. Temperature was calculated as a function of radial distance r from the beam center.	60
A-2	Temperature rise at the center of laser spot calculated using an infinite sheet model as a function of time when the 1 W laser is focused to the spot of diameter 43 μm	61
A-3	Dimensionless temperature profile calculated using an infinite sheet model after time t s of the laser irradiation.	61
A-4	Schematic of heat transfer model. Heat flux from the substrate to its holder is assumed to be proportional to their temperature difference.	62
B-1	A schematic of the semiconductor laser and its focusing optics.	65

B-2	Reflection and transmission of plane wave.	66
B-3	An incoming wave whose electric field is (a) normal to the plane of incidence and (b) in the plane of incidence.	68
B-4	Reflectance and transmittance of a Si wafer at 977 nm wavelength as a function of incident angle.	71

1. Introduction

Microelectronic devices are universally built from patterned thin films or patterned substrate materials. Photolithography, which consists of spin-coating of the photoresist, exposure to light, development, and baking, is the technique by which most of the patterns are made. After the lithography step, the parts of the substrate are covered by the photoresist, which literally resists the following treatment. A certain pattern will be transferred to the substrate by an additional (e.g., oxidation, ion implantation) or subtractive process (etching). This patterning technique using lithography is a multistep process, and it processes the entire substrate surface at the same time.

Use of Focused ion beams (FIB) can alter the conventional wafer process entirely by eliminating the optical lithography step. FIB fabrication is a serial process, and it processes only a part of the substrate at a time. Therefore, this technique is slow in treating the whole substrate surface. Nevertheless, the FIB technique may provide far better flexibility to microelectronic fabrication: a transistor can be implanted point-by-point, or a part of the metal conductor on the wafer can be added or subtracted.

In this chapter, conventional lithography techniques are reviewed with a focus on the limitations of these techniques in applications for submicron devices. Then, FIB systems are discussed, with emphasis on the ion beam resolution. Ion beam induced deposition will be discussed, from the theoretical and practical points of view, in the subsequent section on FIB applications. Finally, the objective of this research will be presented.

1-1 Photolithography

Since the first transistor was invented at Bell Laboratories in 1947, semiconductor device technologies have grown rapidly. Many breakthroughs have been

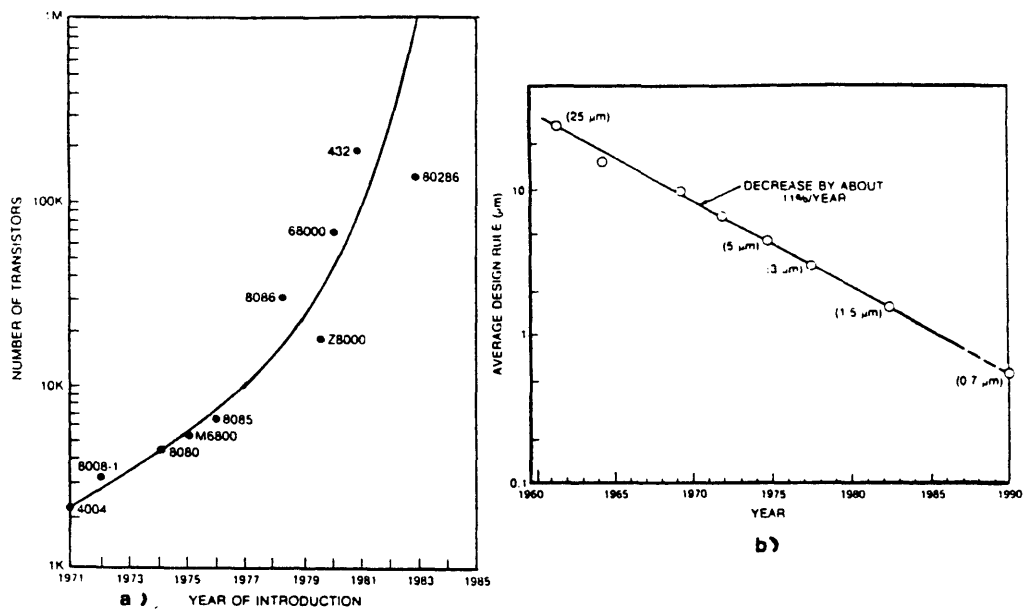


Figure 1-1: (a) Increase in the number of transistors per microprocessor chip versus year of introduction, for a variety of 8-bit and 16-bit microprocessors, and (b) the decrease in minimum device feature size versus time on integrated circuits [1].

made in semiconductor device fabrication such as alloy-junction and grown-junction techniques, zone-refining, diffusion, epitaxial growth, beam-lead, ion-implantation, sub-micron lithography, and dry-etching technologies. One of the clearest indications of technological advancement is the number of devices manufactured on a chip. As shown in Fig. 1-1a, the number of transistors has increased exponentially and this trend is expected to continue in the foreseeable future[1]. This increasing number is attributed to a shrinking minimum feature size as shown in Fig. 1-1b. Submicron devices have been developed in the late 1980s and commercially available since the early 1990s.

In very large scale integrated circuit (VLSI) fabrication, the resolution of the optical lithography system is of major importance because it is the main limitation controlling the minimum device size. The basic steps of conventional lithography techniques are shown in Fig. 1-2[1]. First, a thin layer of photochemically active

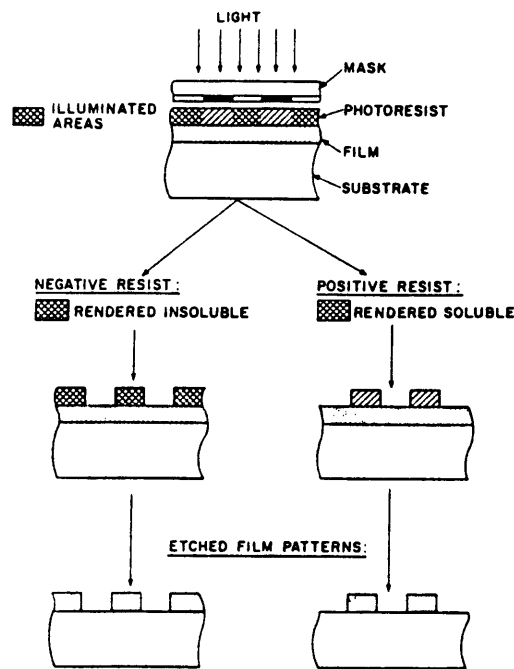


Figure 1-2: Exposure and development of negative and positive photoresists, and resulting etched film patterns [1].

photoresist or simply resist, is spin-coated on the wafer substrate. The resist layer is then selectively exposed to a form of radiation, such as ultraviolet light, electrons, x-rays, or ions. The patterns in the resist are formed by removing a part of the resist layer after the development step. The areas of resist remaining on the substrate protect the substrate regions which they cover. The uncovered areas are subjected to a following additive or subtractive process that transfers the pattern onto the substrate surface. Oxidation, diffusion, ion implantation, and metalization are examples of the additive processes, and wet and dry etching are examples of subtractive processes.

It is easily understood that in order to fabricate a submicron device, lithographic processes with submicron spatial resolution must be available. This resolution can be limited by several factors, such as diffraction of light, lens aberrations, mechanical stability of the system, optical and chemical properties of the resist. In any optical projection system, the major factor that limits its resolution capabilities is the physical

design of the objective lens and its numerical aperture (NA). The NA is a measure of a lens' capability to collect diffracted light from an object (mask) and project it onto the wafer. The NA is defined by

$$NA \equiv n \sin \alpha$$

where n is the refractive index (typically 1.0 for air) and 2α is the angle of acceptance of the lens. The NA of lenses in practical projection aligners ranges between 0.16-0.40.

The resolution of lens' depend on the wavelength and the degree of coherence of the incident light, and the NA of the lens. The definition of the resolution is based on Rayleighs criterion. That is, diffraction causes even a geometrically perfect lens to image an ideal infinitesimally small point source into a blurred disc, called the airy disc. When two points are so close that the two airy disks look like a single blurred disk, the two points cannot be resolved. Rayleighs criterion defines two images as being just resolved when the intensity between them drops to 80% of the image intensity. Mathematically, this criterion is expressed as

$$2b = \frac{0.61\lambda}{NA},$$

where $2b$ is the separation distance of two images and λ is the wavelength of the light. For example, the Rayleigh limit of the minimum resolvable dimension is $0.47 \mu\text{m}$ when the G-line of the mercury-arc spectrum ($\lambda = 436 \text{ nm}$) is used as a light source with a lens of $NA=0.28$.

A larger NA would allow a larger angle of collection and therefore better resolution. However, the depth of focus, d , is inversely proportional to the square of the NA,

$$d = \frac{\lambda}{(NA)^2}.$$

For example, for $NA=0.28$ and $\lambda = 436 \text{ nm}$, $d=5.60 \mu\text{m}$. It can be seen that variations in the substrate flatness could readily distort the images on the surface. Therefore, it is necessary to choose an appropriate NA to achieve the design rules.

One of the strategies to extend practical resolution in VLSI devices obtainable with optical lithography is to reduce the wavelength since the resolution is proportional to the wavelength. The I-lines of the mercury-arc spectrum ($\lambda=365$ nm), KrF ($\lambda=248$ nm), and ArF ($\lambda=193$ nm) excimer lasers are being used as a light source for sub-micron devices. Multilayer resist imaging has developed as an alternative to single-layer resist processing since the use of high-NA lenses with shallow depth of focus has made sub-micron imaging in relatively thick resist layers difficult[2]. Multilayer resist imaging helps to solve the problem by providing an initial coating that effectively planarizes the wafer topography. This is followed by a second coating that is typically much thinner and serves as the pattern-forming layer through which the underlying layer is exposed and then developed or etched. It has been demonstrated that the use of phase-shifting masks can increase the resolution and depth of focus. A phase-shifting mask has a transparent phase-shifting layer covering adjacent apertures so that the light coming from one of the feature is delayed so that it arrives 180 degree out of phase. The two diffracted beams will cancel and desired dark area between images will be obtained[3]. Optical lithography has been the backbone and mainstay of the world's microchip production activity, and it is predicted that optical lithography, with these advanced technologies, will most likely continue in this dominant role until about 1997[4].

1-2 Focused Ion Beam System

Ion beams can be used in the focused ion beam (FIB) and showered ion beam (SIB) modes. Etching, sputtering, and ion implantation are all examples of processes that use SIB technology. Ion lithography, direct ion implantation, local etching and deposition are examples of FIB technology. Significant research activity is ongoing in the U.S., Japan, and Europe to capitalize on the potential advantages of the FIB technique[5][6].

A typical FIB system consists of an ion source, a blanking system, deflectors to

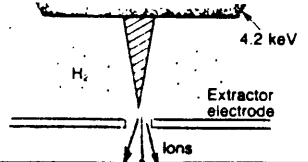
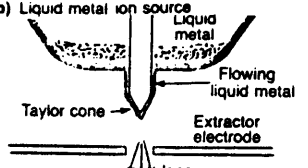
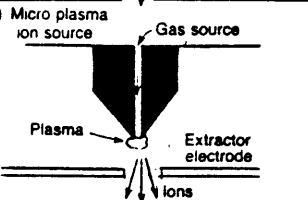
Source type & Schematic	General Source Characteristics	Brightness (B) (A cm ⁻² sr ⁻¹)	Energy spread ($\frac{\Delta E}{E}$) (eV)	Angular current density (μAsr^{-1})	Virtual Size	Typical ions
(a) Gas-field ion source 		10 ⁶	1	10-50 μAsr^{-1}	≈ 10 Å	H ₂ ⁺
(b) Liquid metal ion source 		10 ⁵	5-10	10-50 μAsr^{-1}	100-500 Å	Li Ga Au
(c) Micro plasma ion source 		10 ³	5	3 mAsr^{-1}	50 μm	H He Ar

Figure 1-3: Three basic ion sources and their characteristics [4].

guide the beam over the wafer, electrostatic lens for imaging the beam-defining aperture over the wafer, and a channel electron multiplier (CEM) to monitor the substrate surface[7]. The primary components of recent focused ion beam systems are reliable ion sources. Three types of sources are currently used: a) gas field sources; b) liquid metal sources; and c) plasma sources. Fig. 1-3 shows the three basic ion sources and their characteristics[7]. The desired ion sources are those that emit ions from a single point into a limited solid angle with a high ion current. Liquid metal ion sources (LMIS) have become the most widely used ion sources to date due to their smaller spot sizes and availability of various dopant materials for Si and GaAs.

A LMIS typically consists of a fine tungsten capillary or of a capillary with a tungsten needle projecting through it[8]. The operation of the source involves feeding liquid metal to the tip of the capillary tube and applying a voltage between the tip and the

extractor electrode. The interaction between electrostatic and surface tension forces causes the liquid metal meniscus to form a sharply peaked cone of small radius (Taylor cone). The critical voltage to form a Taylor cone is typically around 10 kV[8]. At the critical voltage, the cone has a half-angle of 49.3 °. The radius of the tip was measured to be less than 100 Å[9]. Space charge or viscosity of liquid metal limits the emission current, and the Taylor cone is pretty stable over long times of operation[10]. Among the elemental and alloy sources, Ga is most commonly used since it is almost liquid at room temperature and yields a long emitter life span[11].

The limits of LMIS performance are largely determined by the electrostatic repulsion of the ions[11]. An ion leaving the tip is influenced by the nearby ions in addition to the applied electric field. Since the locations of the other ions are random, the influence due to the nearby ions are also random. The ion is therefore randomly accelerated or decelerated in radial and axial directions. The component of fluctuation normal to the ion beam axis contributes to a virtual source that could be ten times larger than real size of LMIS. The component parallel to the beam results in the variation in the energy of ions, ΔE . Generally, ΔE is higher for heavier ions. Typically, ΔE at 10 μ A of source current is 10, 15, and 24 eV for Al, Ga, and Au, respectively[12].

An electrostatic lens for imaging is very much like optical lens systems which focus a photon in place of ions for an electrostatic lens[8]. An electrostatic lens for ions consists of two or more very precisely machined washer-shaped electrodes at high potentials. The ion beam passes through these electrodes and is deflected and accelerated by the electric field as shown in Fig. 1-4.

One of the properties which limits the operation of an electrostatic lens is chromatic aberration; that is, the lens has a different focal length for different ion-energies. This leads to the most serious practical limitation to the performance of most present FIB columns[11]. The chromatic aberration would cause an otherwise point source to have a diameter,

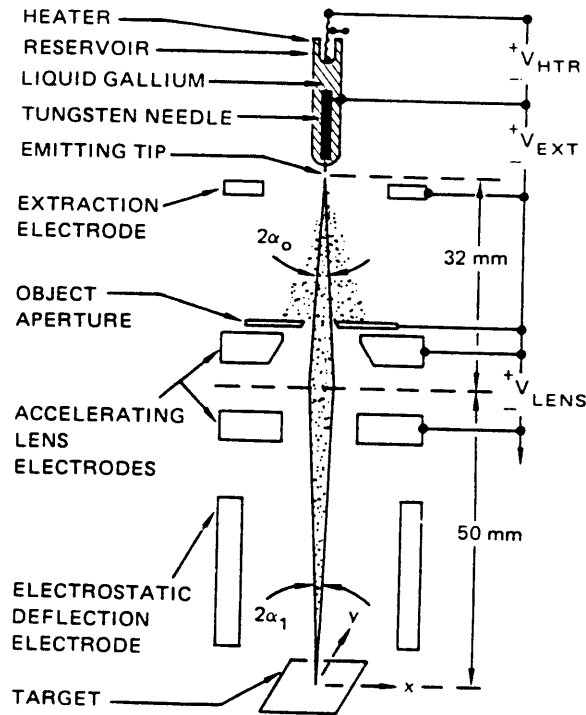


Figure 1-4: Schematic diagram of focused ion beam optics [5].

$$d_c = C_c \alpha \frac{\Delta E}{E},$$

where C_c is the chromatic aberration coefficient, α is the half-angle of the beam, and E is the ion energy[11].

Spherical aberration is another cause of increased beam diameters. It is caused by the non-ideal radial dependence of the focusing fields of a lens. The contribution to beam diameter due to spherical aberration is,

$$d_s = \frac{C_s \alpha^3}{2},$$

where C_s is the spherical aberration coefficient. Since α is typically on the order of 1 mrad, this effect is negligible in most cases.

The other important effect which contributes to the finite diameter of an ion beam is the virtual source diameter d_0 as discussed above. The total diameter of the beam spot at the exit of the ion column is given by

$$d = \sqrt{d_0^2 M^2 + d_c^2 + d_s^2},$$

where M is the magnification of the lens. When α is under 1 mrad, the virtual diameter is a dominant term limiting the beam diameter.

A beam blanker is used to turn the beam on and off. A typical beam blanker consists of a pair of electrodes on opposite sides of the beam. The beam is deflected sideways by applying the voltage between the electrodes. The angle of deflection needed to turn off the beam is the ratio of the transverse velocity caused by the deflector to the velocity along the beam axis, and it is typically on the order of 0.5 mrad. The beam blanker is also used in conjunction with a deflector to write certain patterns on the substrate.

The ultimate resolution of any patterning done with FIB will depend on the beam

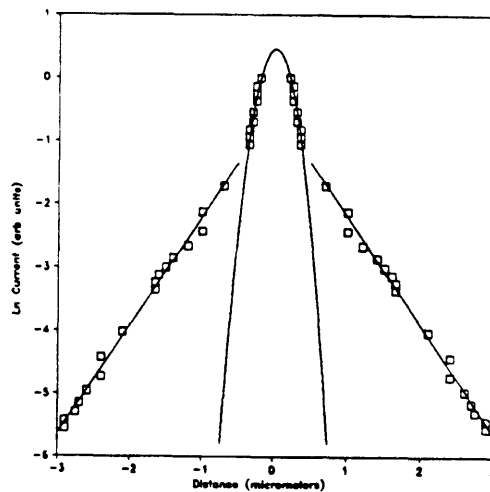


Figure 1-5: Plot of natural log of the current versus distance from the center of the beam [13]. The squares are measured data, the center curve is the Gaussian fit (FWHM = 0.5 μm) and the lines are fits to the exponential tails.

profile. The current density in the ion beam spot focused on a sample is generally thought to have a Gaussian profile. However, it has been shown that much a higher current density than predicted is observed below the 2 to 3 orders of magnitude lower than the peak intensity (ref. Fig. 1-5) [13]. If high contrast between the two adjacent areas is very important, these skirts in the beam profile must be taken into consideration.

1-3 Focused Ion Beam Application

Energetic ions cause various physical and/or chemical effects on irradiated materials. These effects are present in several categories of applications, such as ion implantation, milling, surface chemical reaction, lithography, microscopy, and materials analysis. First in this section, interaction of ions with matter will be discussed. Then, several FIB applications will be presented.

The interaction of energetic ions with solid materials has been extensively studied in the area of ion implantation. The mechanism by which ions lose their energy and the spatial distribution of ions in materials, especially in Si and GaAs, are well understood [14]. There are two basic stopping mechanisms by which energetic ions can be brought to rest in a semiconductor material. The first one is interaction with the target atomic nuclei and the other is that with the bound and free electrons in the target.

The average rate of energy loss with distance is given by

$$-\frac{dE}{dx} = N[S_n(E) + S_e(E)],$$

where E is the ion energy, x is the distance from the wafer surface (normal to the surface), N is the number of target atoms in a unit volume, and S_n and S_e are stopping powers due to nuclear interactions and to electronic interaction, respectively[14]. The approximate stopping power for amorphous materials is given by

$$S_n \propto \left(\frac{Z_1 Z_2}{\sqrt{Z_1^{2/3} + Z_2^{2/3}}} \right) \left(\frac{M_1}{M_1 + M_2} \right),$$

where Z is the atomic number, and M is the atomic mass, with subscripts 1 and 2 denoting an incident ion and a stationary particle in the target, respectively. The electronic stopping is, by considering the collision of an incident ion with a free electron gas, expressed as

$$S_e = k\sqrt{E},$$

where k is a material dependent constant[14].

In general, the ion distribution in the target is given by

$$N(x) = \frac{Q_0}{\sqrt{2\pi}\Delta R_p} \exp\left[-\frac{1}{2}\left(\frac{x - R_p}{\Delta R_p}\right)^2\right],$$

where Q_0 is the ion dose, R_p is the mean value of the distance traveled by the ions, or the projected range, and ΔR_p is the standard deviation from R_p , or the straggle. The profile can be dramatically altered if the incident beam is aligned along a low index crystallographic axis. This gives rise to a process called channeling, by which ions travel a considerable distance through the target lattice with little energy loss[14].

In the discussion above, we have focused on how an ion loses its energy and imbeds itself in the target material. In addition, the ion produces other changes in the substrate: a) radiation damage results from the displacement of atoms from their lattice sites due to collisions with the ions; b) substrate atoms are also sputtered, that is, they are removed from the substrate due to collisions with the incident ions; c) electrons are also emitted when an ion strikes the surface; and d) local heating, or thermal spikes, may be caused by ions, lasting of order 10^{-10} to 10^{-11} s.

Many FIB applications which result from a number of effects caused by incident ions have been developed. Among various applications, ion beam milling, lithography, doping, and deposition and etching (Fig. 1-6) will be discussed here since FIB is thought to be a useful tool in these areas. FIB, in which the beam diameter can be less than 0.1 μm , offers a radical departure from the conventional fabrication process. By using an FIB, it may be possible to fabricate a device without using a single mask.

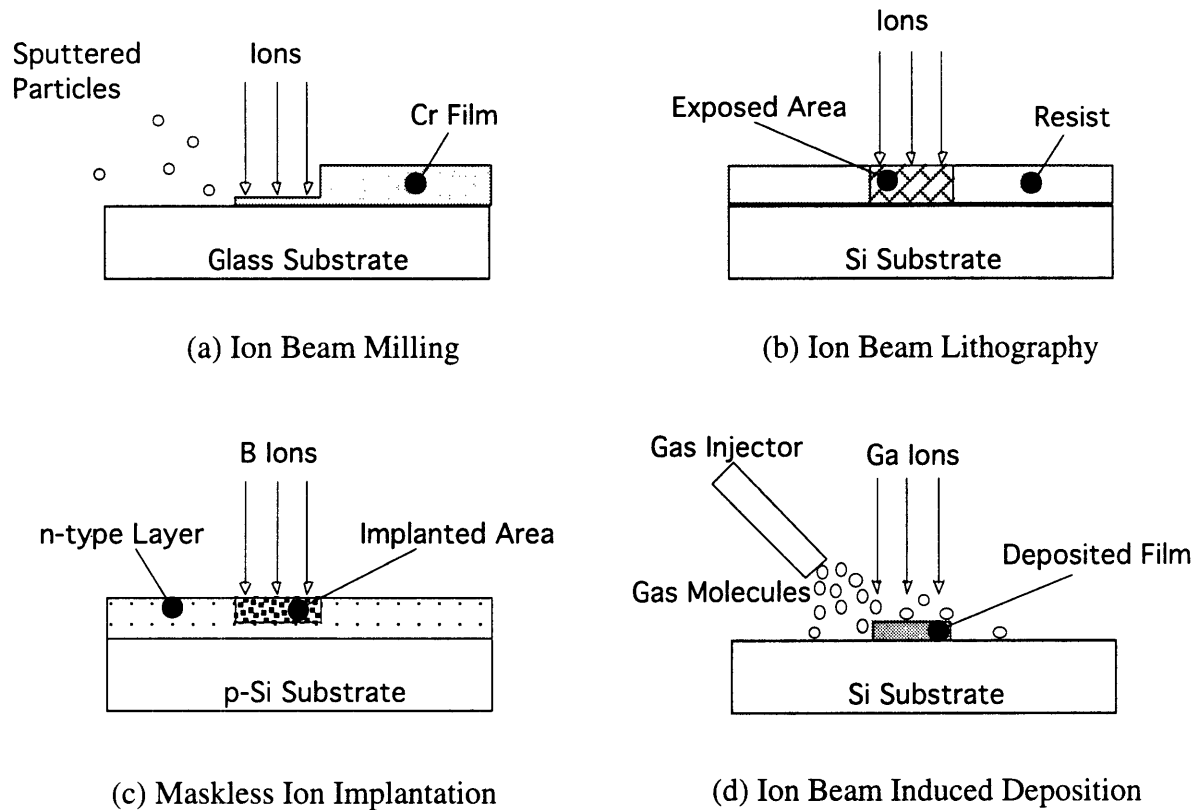


Figure 1-6: Schematic diagram of (a) ion beam milling, (b) lithography, (c) maskless ion implantation, and (d) ion beam induced deposition

Ion milling is one of the widely used techniques in microfabrication to remove materials from the substrate. In FIB, ions of a few tens of keV energy are incident on a surface, and remove material only by sputtering without any chemical reaction. Therefore, only the material within the beam diameter may be removed. The number of removed atoms per incident ion, or yield, is typically one to two, and it increases as the ion energy is increased up to 50 keV[11]. The most common application of FIB milling is the repair of opaque defects on a photomask (i.e., removal of Cr from areas in which they do not belong for optical photomasks and Au for x-ray photomasks). The other application of this technique includes circuit microsurgery such as cutting conductors, sensing the voltage in an integrated circuit, or removal of passivation layer to make a via holes.

The use of ions in lithographic processes is also under consideration, due to their potential advantages compared with optical and electron beam lithography techniques. As discussed above, optical lithographic techniques have physical limitations in printing tiny features deep in the submicron range. Electron beam lithography may be used in this range. However, charging problems for mask fabrication are severe since the pattern consists of a large number of isolated structures on a glass substrate. In addition, electron beams suffer from forward and back scattered electron interaction with the atoms of the resist and substrate. The sensitivity of resists to electrons is not as high as that to ions. Ion beam lithography is very attractive for these reasons in microfabrication. FIB makes direct writing, making a pattern on the substrate without using a mask, possible. FIB doping is essentially the same as conventional ion implantation. Due to the small beam size of focused ion beams, maskless ion implantation may be possible in submicron areas.

In ion induced deposition, a local gas ambient in the millitorr range is created at the substrate surface around the point of ion incidence, typically by using a tiny capillary as shown in Fig. 1-6(d). Much has been published in this field, including a number of reviews[17][18][19]. A schematic of the ion-beam induced deposition process is shown in Fig. 1-7. Incident ions decompose the reactant molecules, typically metal organic compounds or metal halides, that are adsorbed on the surface. The decomposed molecules are desorbed from the surface leaving metal atoms and often carbon and oxygen impurities. It was shown that the decomposition yield, the number of molecules decomposed per incident ion, as well as the net deposition yield is increased with increasing ion mass and energy, and is approximately proportional to the nuclear stopping power[20].

Two mechanisms by which a reactant gas is decomposed by ions have been proposed [20] for the FIB-induced deposition of gold from the dimethyl gold hexafluoroacetate (DMGH). One is a binary collision model and the other is a thermal

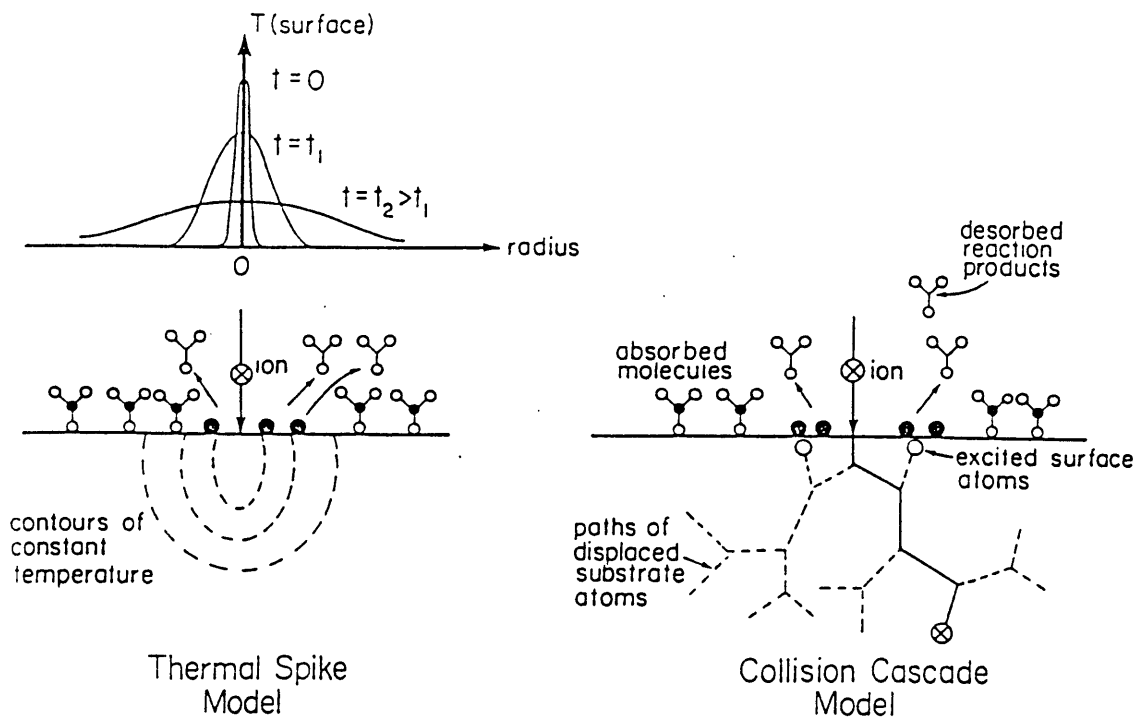


Figure 1-7: Schematic of (a) the binary collision model and (b) the thermal spike model[19].

spike model. Schematics of the binary collision model and thermal spike model are shown in Fig. 1-7. In both models, the decomposition process is thought to be substrate mediated; the energy lost by incident ions excites the local area of the substrate where the ions are centered, and the substrate in turn causes the adsorbed molecules to break up.

In the binary collision model, an incident ion scatters and displaces lattice atoms, forming "collision cascades." When these collision cascades intersect the substrate surface, surface atoms acquire energy. If the energy is above the sputtering threshold (typically, several eV), the surface atoms are removed. If the energy is above a certain threshold (the thermal activation energy, 0.95 eV, in case of DMGH), the adsorbed molecule will decompose. A Monte Carlo calculation using the TRIM-TC simulation program[21] was used to determine the distribution of energetic surface atoms (ESA) N as a function of ESA energy E_0 . The fraction of successful ESA's which decompose

adsorbed molecules, $f(E_0)$, was calculated by evaluating the probability of an ESA striking the different atomic species comprising the molecule. Finally, the decomposition yield was calculated by integrating the product of the ESA energy distribution and the fraction decomposed,

$$Y_D = \int_0^{\infty} N(E_0)f(E_0)dE_0.$$

The results of this binary collision model are in very good agreement with the experimental data, though the predicted yields are slightly smaller than the measured yields.

In the thermal spike model, the temperature in the incident area on the surface is considered to be elevated up to a few thousand degrees C in the order of 10 to 100 ps, and this causes the adsorbed molecule to decompose pyrolytically. There are two major assumptions in this model: (a) the deposited energy by incident ions is distributed among the atoms in the collision cascade such that a local, transient thermal equilibrium is reached, and a temperature can be assigned; and (b) the decomposition mechanism on the small surface and short time scales over which the ion-solid interaction exists and quenches is same as that for conventional thermal chemical vapor deposition. To calculate the deposition yield, a temperature distribution and a reaction-rate must be evaluated. The temperature was calculated by assuming the initial energy distribution to be three-dimensional function, and heat conduction to be hemispherically symmetrical. The reaction-rate was evaluated by assuming first-order reaction kinetics. The deposition yield resulting from the thermal spike model was in reasonably good agreement with the measured yields. The yields predicted for heavier ions, such as Xe^+ and Kr^+ , were in better agreement with the measured yields than those for lighter ions. Though the binary collision model predicted the yields more accurately than the thermal spike model, the thermal spike model can be more attractive in some applications since it is much simpler and easier to apply to the other systems and further refinements might give better agreement.

The characteristics of the deposited films, such as composition, microstructure, resistivity, yield, adhesion, damage, and minimum dimensions have been extensively studied in many materials, such as C[22], W[23][24][25][26], Au[27][28], Pt[29], Al[30], SiO_x[31], and Cu[19]. For applications in circuit repair, the resistivity is one of the most important characteristics to be evaluated. It has been shown that the resistivities reported range up to 2 orders of magnitude higher than the bulk metal values. Impurities, particularly C and O, are thought to be the causes of high resistivities.

Much effort has been made to reduce the resistivity. One simple way is choosing an ideal precursor gas which contains the desired metal that remains on the surface while the other unwanted constituents of the molecule are volatile and are immediately pumped away. Tungsten hexafluoride might fit this model, and indeed a resistivity of 15 $\mu\Omega$ -cm has been reported for FIB-induced deposition of tungsten (5.3 $\mu\Omega$ -cm for bulk tungsten)[23]. This lower resistivity results from the relatively pure composition. The atomic percentages of W, F, and C are 93.3, 4.4, and 2.3, respectively. Unfortunately, this reactant tends to etch the substrate rather than deposit film, and relatively pure tungsten was deposited only when low energy ions were used[23][24].

Another approach is to optimize the dwell time, defined as the length of time when any point on the sample is irradiated by an ion flux. It was observed for Cu deposition that the longer the dwell time, the smaller the resistivity[19]. One explanation is that a form of ion beam-induced annealing is taking place at longer dwell times. The other is that the byproducts, carbon and oxygen, can more readily escape the film since the growth rate is reduced at longer dwell times. This approach has the severe disadvantage in practical use that it is slow, and also the longer the dwell time leads to lower deposition yields[19][32].

To raise the substrate temperature is found to be effective in reducing the resistivity while the deposition yield remains the same for gold deposition[28], or is improved by a factor of two for copper[19]. The resistivity of gold films deposited

above 120 °C, and that of copper above 100 °C, are very close to the bulk values, 2.4 and 1.7 $\mu\Omega\text{-cm}$ for Au and Cu, respectively. Through TEM analysis of the films, the Cu microstructure was found to have become more coarse and dense as the deposition temperature was increased. It was also confirmed by using Auger Electron Spectroscopy that the relative ratio of metal to other impurities increases at higher temperature. These two effects contribute to the lower resistivity. In both cases, however, substantial stage drift due to substrate heating was reported. Wider line widths at higher temperature were thought to be due to this stage drift.

1-4 Objectives

The research reported in this thesis is focused on FIB-induced copper deposition from copper hexafluoroacetylacetonate trimethylvinylsilane, abbreviated Cu(hfac)-TMVS. A semiconductor laser was used in conjunction with the FIB system to locally heat the substrate. The main objective of this paper is to assess the feasibility of the uses of a local heating system to achieve both low resistivity and high yield while maintaining the same spatial resolution of lines deposited at lower temperatures. The following issues are clarified:

- (a) the feasibility of local heating in an FIB-induced deposition system,
- (b) the deposition yield and growth rate under locally heated conditions,
- (c) the electrical characteristics of the deposited films, and
- (d) whether improved line width control is possible with local heating.

The major parameter in this research is the output power of the semiconductor laser, of which the maximum power is 1.2 W at the wavelength 977 nm. As will be discussed, the laser power can be converted to a local temperature of the surface of the substrate on growing film.

2. Experiments

This chapter will outline the experimental equipment and procedures for the focused ion beam (FIB) induced deposition of copper. The FIB system, including its vacuum system, will be discussed here. The semiconductor laser used to heat the substrate locally will be presented with emphasis on optics and spatial resolution. The use of a new copper precursor, copper hexafluoro-acetyl-acetonate trimethyl-vinyl-silane, is also discussed. The general experimental procedures, such as deposition, yield and resistivity measurements, are described in detail.

2-1 Focused Ion Beam System

The focused ion beam (FIB) system used in these experiments is a 25 kV FIB 500D Focused Ion Beam Milling System manufactured by FEI company, Beaverton, OR. The system block diagram is shown in Fig. 2-1[33]. The ion focusing column, mounted on top of the specimen chamber, consists of a liquid metal ion source (LMIS), two electrostatic lenses, one set of beam blanking plates, a beam defining aperture, and two octupole deflectors. The column is evacuated by an ion pump and operates in a high vacuum condition ($<5 \times 10^{-7}$ torr) to avoid interference with the beam from gas molecules, and to maximize the lifetime of the LMIS. Gallium liquid is used as the ion source material, and has a current/lifetime product of 1500 $\mu\text{A}\cdot\text{hr}$, if operated under modest emission current ($<10 \mu\text{A}$). The ion beam diameter at the working distance of 25 mm is estimated to be 320 Å when the beam voltage is 25 kV and the smallest aperture (48 μm in diameter, or 0.49 mrad in beam semi angle) is selected.

A small orifice between two chambers allows the beam to pass out of the column into the specimen chamber when a valve connecting the chambers is open. When closed, the valve isolates the specimen chamber from the column which maintains the

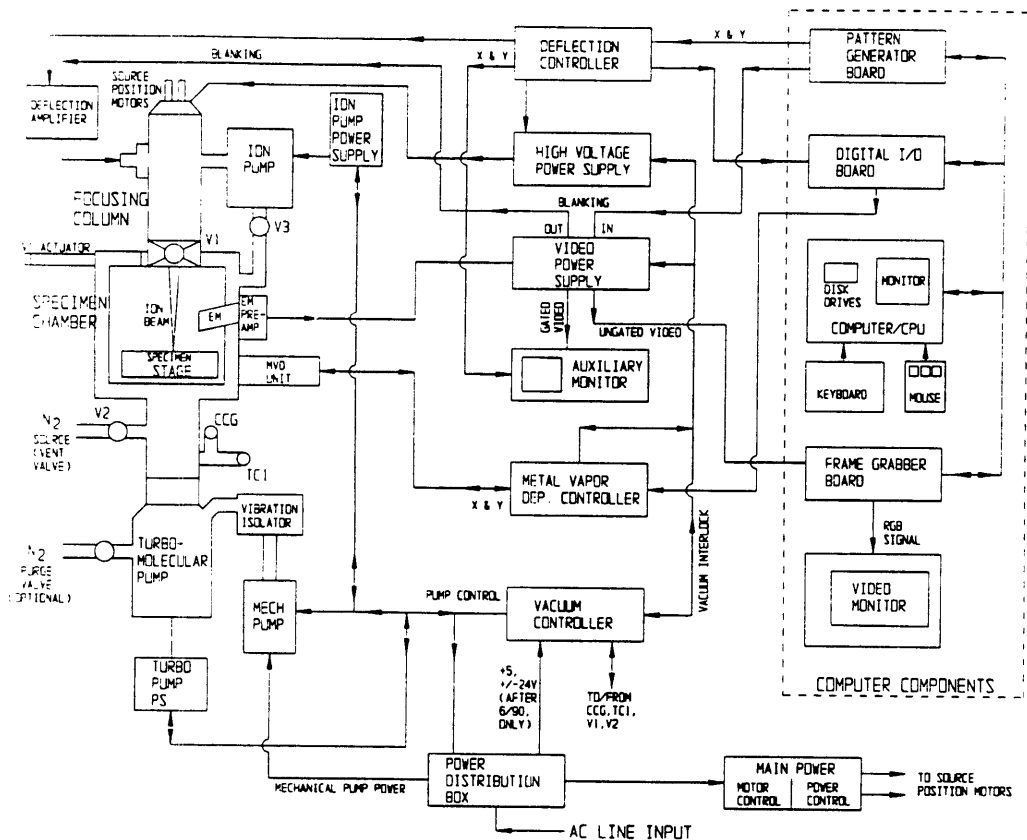


Figure 2-1: The FIB system, FEI 500D, block diagram[33].

pressure in the column while venting the chamber. Differential pumping enables the column to maintain one to three orders of magnitudes higher vacuum than the specimen chamber, which is evacuated by a turbo-molecular pump.

A schematic of the specimen chamber is shown in Fig. 2-2. A sample is put on the substrate holder that is tilted 45 degrees so that both the ion and the laser beams hit the sample at this angle. The sample stage may be moved in three directions and tilted up to 45 degrees. A cylindrical lens is also placed on the stage 150 mm away from the sample. The photodiode behind the substrate holder is used to align the laser beam before deposition. The precursor gas is introduced to the chamber via a tube of which one end is connected to the 0.8 mm inner diameter capillary. This provides a millitorr

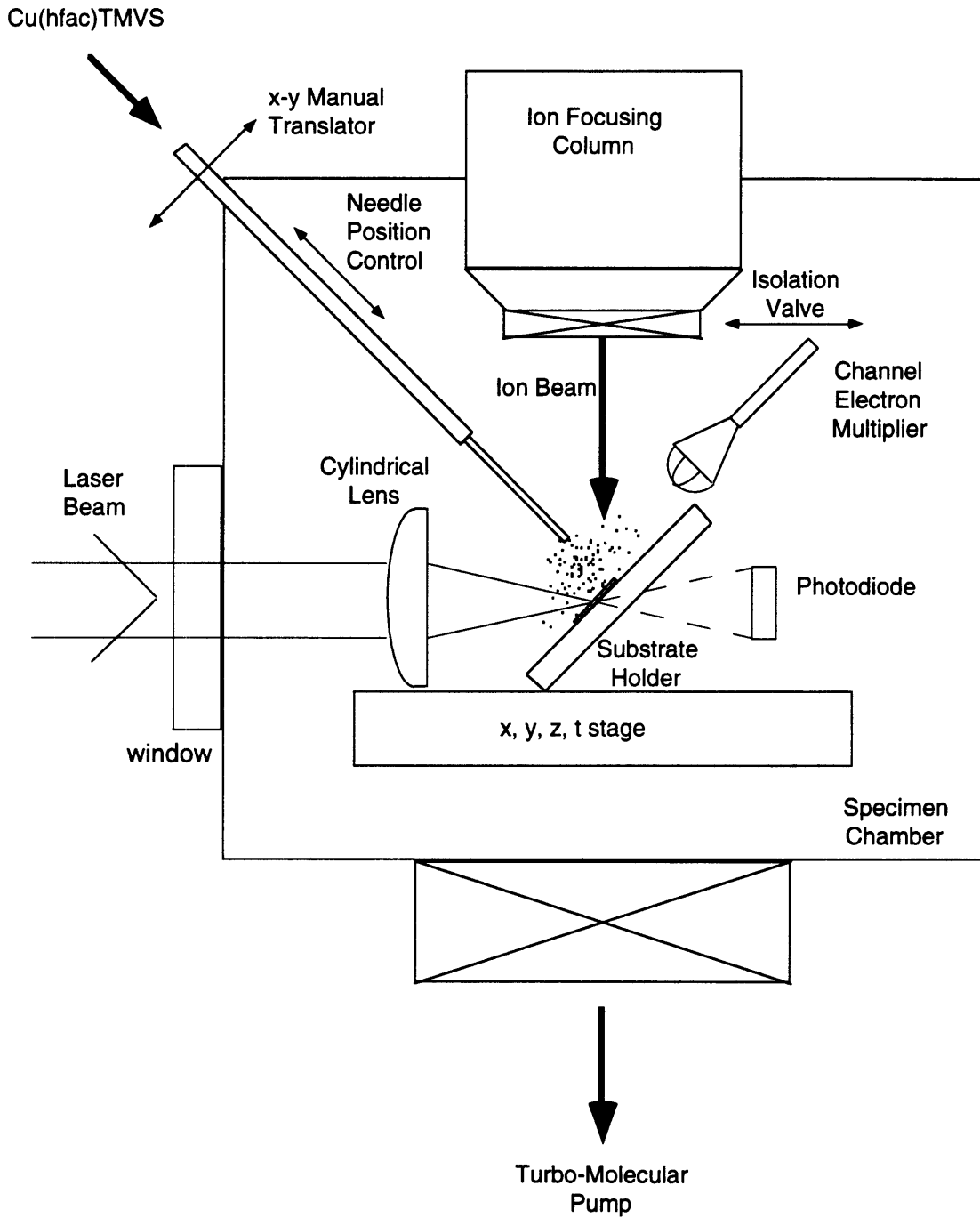


Figure 2-2: A schematic of the specimen chamber.

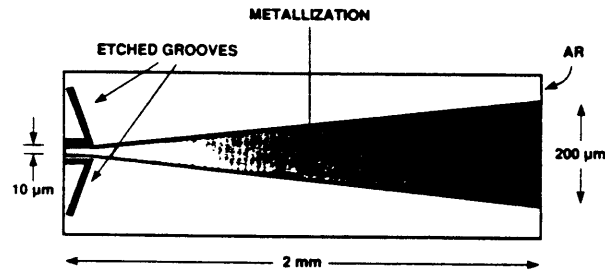


Figure 2-3: Junction-side-up view of the semiconductor laser with tapered contact region and etched grooves to spoil the cavity[34].

ambient of the precursor on the substrate while the chamber maintains a relatively high vacuum ($<5 \times 10^{-6}$ torr). The channel electron multiplier unit collects secondary ions and electrons, depending on the polarity of the collector, emitted from the substrate when the ion beam strikes the surface. The signal detected by the multiplier is amplified and used to monitor the surface.

2-2 Semiconductor Laser and Optics

The semiconductor laser used in this experiment is fabricated in a InGaAs/AlGaAs, strained-layer, graded-index, separate-confinement heterostructure (GRINISCH), containing a single 5 nm wide quantum well, fabricated at Lincoln Lab, M.I.T.[34]. The laser has been grown on a GaAs substrate by low-pressure organometallic vapor phase epitaxy[35]. The tapered geometry, as shown in Fig. 2-3[34], allows high output powers and efficient energy extraction while maintaining the spatial beam quality. The cw output of 1.3 W has been obtained at the laser current of 2.5 A at 977 nm wavelength, as shown in Fig. 2-4[36]. The laser current has been kept below 2.5 A so that the device is not damaged during operation for long times. Since the semiconductor laser is very sensitive to the operating temperature, it is kept under 16 °C by immersing the laser holder in a methanol bath cooled with a fan.

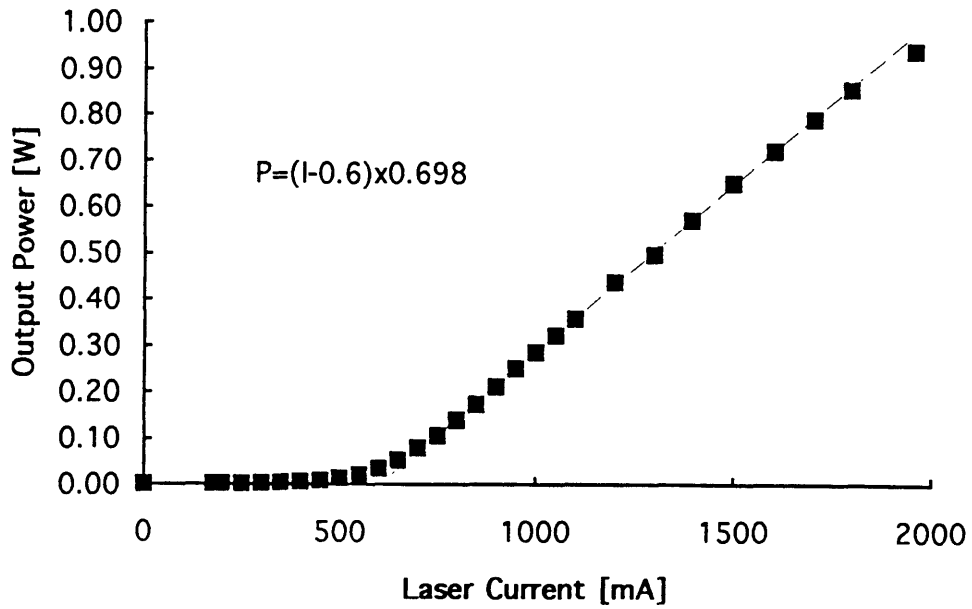


Figure 2-4: The output power measured at the output window with an anti-reflection coating. Shown as a function of the diode current for the InGaAs/AlGaAs heterostructure laser at room temperature.

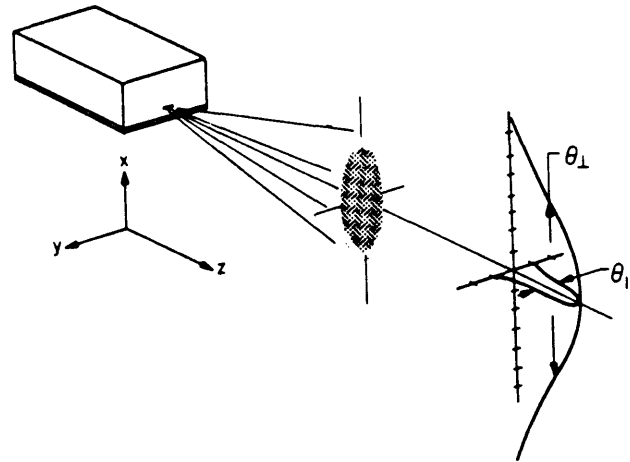


Figure 2-5: Schematic representation of far-field emission of a stripe-geometry double-heterostructure laser[37].

The far-field pattern is the intensity of the emitted radiation in free space. Fig. 2-5 gives a schematic representation of the far-field emission of a typical double heterostructure laser[37]. The full widths at half maximum (FWHM) are θ_{\perp} and θ_{\parallel} in the directions perpendicular to (fast axis) and along the junction plane (slow axis), and they are approximately 45° and 10° , respectively. It should be noted in optical settings that the waist of the laser beam along the fast axis lies at the edge of the laser, while that along the slow axis is virtually located at 0.57 mm inside the edge.

The laser is first collimated along the fast axis and then focused using a cylindrical lens (150 mm focal length). The collimator used here is a Fujinon Diode Collimator SZ394B-2 (17.6 mm focal length and 1.3 focus number). Since the virtual beam waist along the slow axis lies $\delta = 0.57$ mm inside the output window, the beam along the slow axis is focused at S_2 , where

$$S_2 = \frac{f_0(\delta + f_0)}{\delta} \cong 561[\text{mm}],$$

and where f_0 is the focal length of the collimator. The focal points along both axis are aligned to meet at S_2 .

The beam profile along the slow axis has been measured by using an optical fiber and photodetector as shown in Fig. 2-6. At the focal point, an optical fiber is scanned along the slow axis over 5 mm using a precision translator. The other end of the fiber is coupled with a silicon photodiode and its signal is transferred to an X-Y recorder via a lock-in amplifier.

Fig. 2-7 shows the far field intensity profile of the output beam along the slow axis. The laser current was 1 A, and optical filters were placed between the collimator and the fiber to adjust the intensity of the focused laser beam. The beam profile can be well approximated by a Gaussian profile,

$$I = I_0 \exp\left(-\frac{x^2}{w_x^2}\right),$$

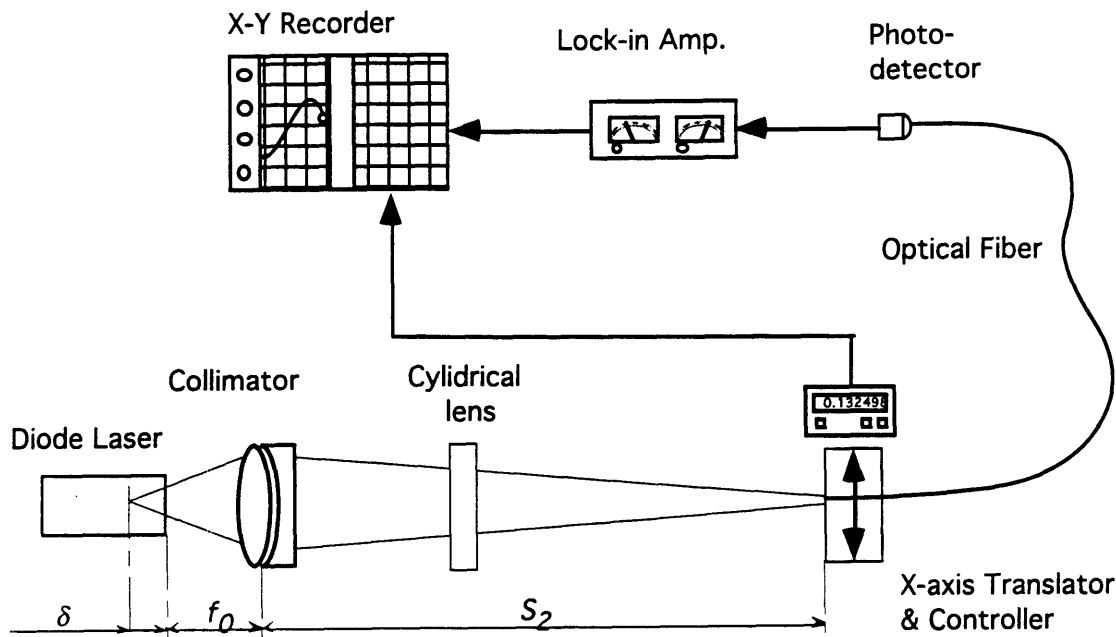


Figure 2-6: Experimental se-up to measure the far field pattern of a semiconductor laser.

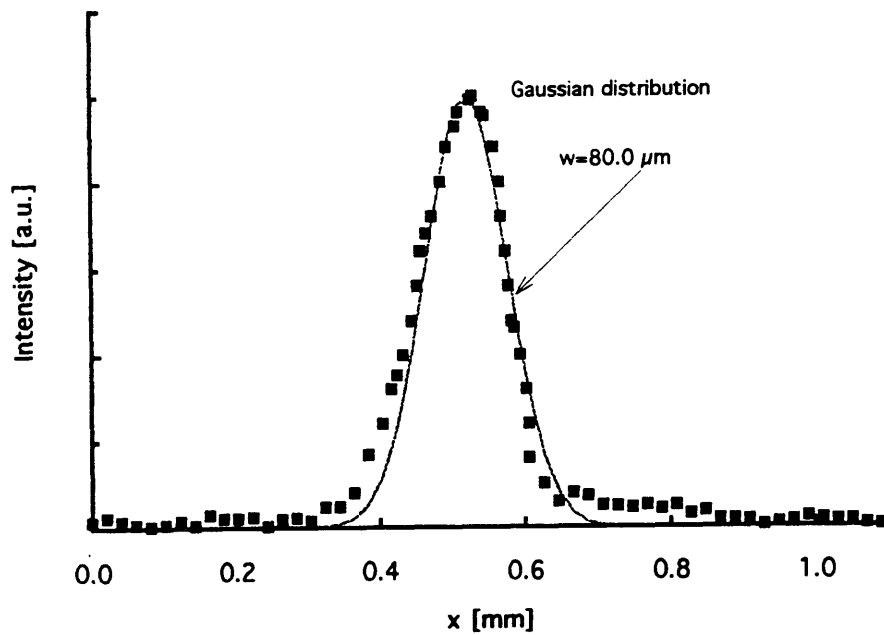


Figure 2-7: The far field intensity profile of the output beam along the slow axis. The Gaussian function was fit to the data.

where I_0 is the intensity at the center of a Gaussian source, x is the distance from the center along the slow axis, w_x is the beam radius along the slow axis where the intensity is I_0/e . The beam radius of the focused beam with the collimator and the cylindrical lens is $80.0 \mu\text{m}$ when the laser current is 1 A. The depth of focus which is arbitrarily defined so that the intensity will be reduced by 5% is given by

$$z = \sqrt{\frac{1-0.95}{0.95}} \cdot \left(\frac{2\pi w_x^2}{\lambda} \right) = 9.44[\text{mm}].$$

The far field intensity profile of the output beam along the fast axis, which is perpendicular to the junction plane, may be calculated assuming a Gaussian beam passing through an ideal lens,

$$I = I_0 \exp\left(-\frac{y^2}{w_y^2}\right),$$

where y is the distance from the center along the fast axis, and w_y is the beam radius along the axis where the intensity falls to I_0/e . The focused spot radius w_y may be approximated by

$$w_y = f\theta_y = f \frac{\lambda}{2\pi w_{0y}} = 4.9[\mu\text{m}],$$

where f is the focal length of the cylindrical lens ($f=150 \text{ mm}$), λ is the wavelength ($\lambda=0.977 \mu\text{m}$), w_{0y} is the beam radius along the slow axis at the cylindrical lens ($w_{0y} = 6.75 \text{ mm}$) [38]. The depth of focus along the fast axis is given by

$$z = \sqrt{\frac{1-0.95}{0.95}} \cdot \left(\frac{2\pi w_y^2}{\lambda} \right) = 35.4[\mu\text{m}].$$

Since the distance from the cylindrical lens to the substrate could be different from the focal length by as much as 0.5 mm, the actual focused beam size could be

$$w_y'(z) = w_y \sqrt{1 + \left(\frac{\lambda z}{2\pi w_y^2} \right)^2} = 16.6[\mu\text{m}].$$

Therefore, the focused spot area on the substrate which is tilted 45 degree is

$$A_0 = \frac{\pi w_x w_y'}{\cos 45^\circ} = 5.90 \times 10^{-5} [\text{cm}^2].$$

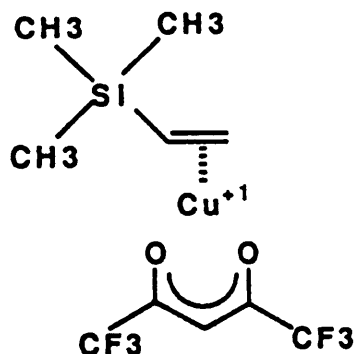


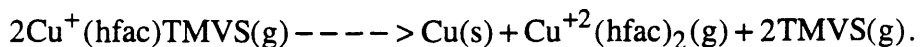
Figure 2-8: Copper (I) hexafluoro-acetyl acetonate trimethyl-vinyl-silane.

The ion beam and laser beam were aligned using a pinhole (100 μm square) which was made on a glass substrate by patterning an evaporated Cr film. First, the pinhole was monitored using the FIB and put at the center of the monitor screen. The laser was then irradiated on the pinhole. The Ge photodiode located behind the sample holder was used to monitor the intensity of the laser beam passing through the pinhole and the holder, which has a 1 mm diameter hole at its center. The laser can be aligned by using an x-y-z translator which is holding the laser collimator, so that the photodiode current can be maximized. Very fine alignment was done by adjusting the tilt of the sample holder within 0.2 degree.

2-3 Copper Precursor

The organometallic complex used in this study is copper hexafluoro-acetyl-acetonate trimethyl-vinyl-silane, abbreviated Cu(hfac)TMVS. Fig. 2-8 shows the molecules structure of the copper compound[39]. The TMVS stabilizes the Cu oxidation state while the compound is either a liquid or a gas under moderate temperature conditions. Under CVD conditions, at more elevated temperatures (>130 $^{\circ}\text{C}$), the TMVS can be made to dissociate, generating unstable Cu(I)(hfac) species which then

disproportionate to yield copper metal and volatile Cu(II)(hfac)₂. The chemical reaction is[39]



Conductors tend to catalyze the above reaction, and selective copper deposition on a variety of conductor/insulator substrates has been demonstrated[39][40]. In all cases, the copper metal selectively deposited on the conductor rather than on the insulators above 120 °C. However, this selectivity can be very sensitive to the surface condition of the substrate, and especially to the cleanliness of SiO₂. Incomplete removal of photoresist and water vapor can lead to loss of selectivity[40].

In this study, the Cu precursor has not been heated up since it has a reasonably high vapor pressure, 0.5 torr, at room temperature. Figure 2-9 shows the Clausius-Clapeyron vapor pressure/ temperature plot[39]. It should be noted that there is no absorption at the 977 nm semiconductor laser wavelength used in this study[41].

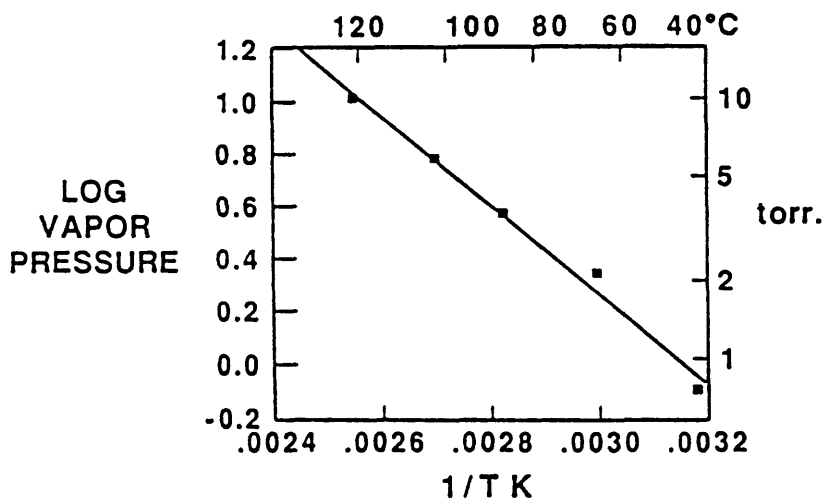


Figure 2-9: Clausius-Clapeyron vapor pressure/temperature plot of Cu(hfac)TMVS

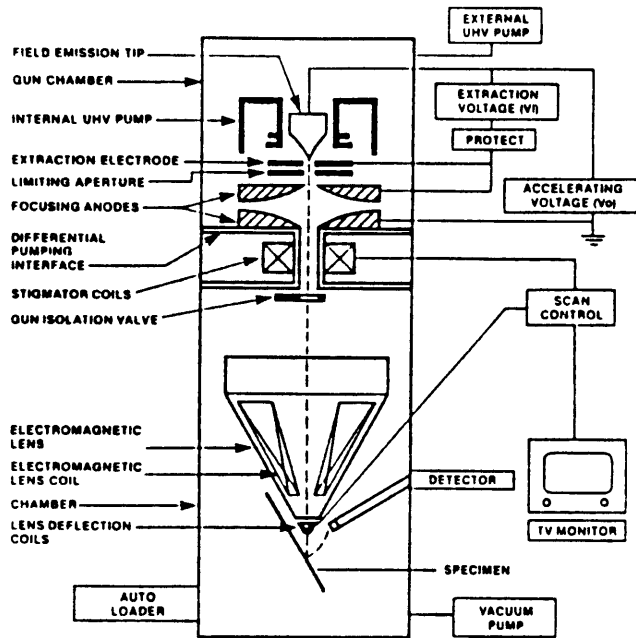


Figure 2-10: Block diagram of an electron optical column of an SEM[1].

2-4 Scanning Electron Microscopy

The scanning electron microscope (SEM) used to analyze the surface morphology was a Cambridge Stereoscan 250 Mk 3. Figure 2-10 shows a schematic diagram of the SEM[1]. A source is used to create a beam of electrons that is accelerated to energies of 500 eV to 40 keV, focused to a small diameter, and directed at the surface of a sample in a raster-scan pattern. The electron striking the surface causes a number of physical phenomena to occur, the most important for SEM applications being the emissions of electrons and x-rays. The emitted x-ray signal is useful for chemical analysis, x-ray emission analysis (XES). The emitted x-ray spectrum contains peaks characteristic of the target, as well as a background continuum.

There are three types of emitted electrons: lower energy electrons of 1-50 eV, peaking at about 5 eV; higher energy electrons, with energies close to those of primary

electrons; and Auger electrons. The lower energy electrons are called secondary electrons and are generally most useful in studying the morphology of the sample surface. The secondary electrons are detected to intensity-modulate the z-axis of a CRT. An image of the sample surface is produced on the CRT screen by synchronously raster scanning the CRT screen and the electron beam of the SEM.

SEM has become an important tool for VLSI analysis because it has the capability of providing much higher magnification, resolution, and depth of focus than optical microscopy[1]. The typical specification for an SEM is as follows: the resolution can be up to 10 Å, the magnification from 10x to 100,000x, and the depth of focus of 2-4 µm at 10,000x and 0.2-0.4 mm at 100x. Since the film thickness of VLSI devices is typically of order of a micron or less, the depth of focus makes SEM's especially useful. SEM analysis yields information on line width, film thickness, step coverage, edge profiles after etch, and other morphology data. In this study, the line width and cross-section have been routinely monitored using an SEM.

2-5 Deposition

The depositions have been carried out on 1000 Å-thick thermally grown SiO₂ on silicon substrates. The base pressure in the specimen chamber and ion column were on the order of 1×10^{-6} and 1×10^{-7} torr, respectively. The copper precursor was introduced into the specimen chamber via a gas capillary (Fig. 2-2). After the gas was introduced, the pressures in the chamber and column rose slightly to 2×10^{-6} and 2×10^{-7} torr, respectively. The local gas pressure on the sample, which was always placed 0.5 mm away from the end of capillary, is assumed to be 0.60 mtorr at room temperature from the previous study by Della Ratta[19]. The relationship between the pressure and the distance from the capillary can be expressed by

$$P_{OM}(x) = P_{OM}(0) \left[1 - \frac{1}{\sqrt{1 + (R/x)^2}} \right]$$

$$= 2.75 \times \left[1 - \frac{1}{\sqrt{1 + (0.4/x)^2}} \right] [\text{mtorr}],$$

where P_{OM} is the pressure of the organometallic gas in mtorr, and R and x are the tube radius and the distance from the tube in mm[19]. The location of the capillary can be easily determined by monitoring the FIB video screen, and the capillary can be moved via three sets of linear translators, one of which is remote controlled and its travel distance can be monitored with a digital indicator.

To initiate the deposition, the scanning area of the ion beam has been confined to a 400 μm line which connects a four-finger pattern. The ions were accelerated by a potential of 25 kV. The current density on the sample tilted at 45 degrees is

$$J = \frac{I_B}{d_B \ell} \cos 45^\circ = 88 [\mu\text{A} / \text{cm}^2],$$

where I_B is the beam current, d_B is the spot diameter, and ℓ is the scanned length. It has been reported that the dwell time strongly influences both the deposition yield and the resistivity[19]. The dwell time, 0.5 μs , was chosen since neither the yield nor the resistivity is sensitive to the dwell time around this value. The FIB conditions used in most of this study are summarized in Table 2-1.

Table 2-1: The FIB conditions for copper deposition

Beam Energy	25 kV
Working Distance	25 mm
Beam Half-Angle (Object)	0.5 mrad
Beam Current	16 pA
Spot Diameter	320 \AA
Scanned Length	400 μm
Dwell Time	0.5 μs

2-6 Yield and Growth Rate Measurement

One of the most important parameters, especially in practical applications, is the deposition yield, or the ratio of the number of deposited atoms to the number of incident ions. The yield has been calculated assuming the atomic density of pure copper. The line width of the deposited copper has been measured using an SEM. The line thickness was measured using a profilometer, a Dektak 8000. A stylus with a mass of 3 mg was traced across a line at a 1-2 $\mu\text{m/s}$ scan speed. This instrument has a z resolution of 20-50 \AA , which is sufficient for use with these deposited films whose thicknesses are on the order of 1000-3000 \AA . The lines are assumed to have rectangular cross sections, making the measured yield somewhat larger than the real yield. The yield is expressed as

$$Y = \frac{whl\rho_{Cu}}{I_B\tau_d / e},$$

where I_B is the ion beam current, τ_d is the deposition time, e is the elemental charge, ρ_{Cu} is the atomic density of copper (8.4×10^{22} atoms/cm³), and w , h , and ℓ are the width, thickness, and length of the deposited line, respectively. The growth rate may be given simply by dividing the thickness by the deposition time.

2-7 Resistivity Measurement

The resistivity is a critical characteristic of the deposited film. A low resistivity shows the film contains little contaminants such as oxygen and carbon[19]. The resistivity is defined by

$$\rho \equiv R \frac{A}{l},$$

where R is the resistance and A is the cross section area of the deposited film. A is calculated assuming a rectangular cross section,

$$A = wh.$$

The resistance has been measured by depositing a 400 μm long line so that the line will connect four fingers as shown in Fig. 2-11. This finger pattern was fabricated using

1000 Å of electron-beam-evaporated gold or Ni/Cr on 1000 Å-thick thermally grown SiO₂ on Si. This facilitates four point probe measurements, which have been made by passing a small fixed current (1 μA to 1 mA) through the outer two pads and measuring the voltage between the two inner pads, which are 100 μm apart. The resistance may be calculated by dividing the voltage by the fixed current, and the resistivity is given by

$$\rho = \frac{V wh}{I l},$$

where V is the voltage, and I is the current. A Hewlett Packard voltmeter and current source were used in the actual apparatus.

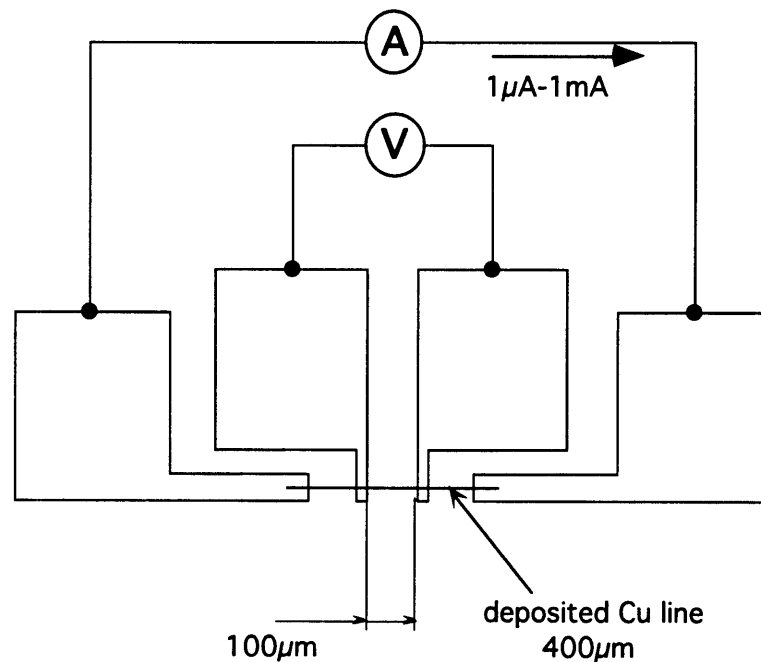


Figure 2-11: Finger pattern used for four point probe measurements.

2-8 Summary

In this chapter, the experimental equipment and procedures for the focused ion beam (FIB) induced deposition of copper have been detailed. The FIB system, including its vacuum system, was described here. The semiconductor laser used to heat the substrate locally was presented with emphasis on optics and spatial resolution. The use of a new copper precursor, copper hexafluoro-acetyl-acetonate trimethyl-vinyl-silane, and its characteristics are also discussed. The general experimental procedures, such as deposition, yield and resistivity measurements, were described in detail.

3. Results and Discussion

The yield, growth rate, resistivity, and microstructure as a function of laser power are discussed in this chapter. The substrate temperature during laser irradiation was measured and calculated with a heat transfer model at various laser powers as a function of time. The resistivities and microstructures of these films are compared with those of the previous studies by Della Ratta[19] and Blauner[28] at equivalent deposition temperatures.

3-1 Substrate Temperature

The temperature rise during laser irradiation was measured with a very fine thermocouple attached to a thermally grown SiO₂ on Si substrate. The thermocouple was made from 75 μm diameter Cu and Cu/Ni Teflon insulated wires. The two wires were soldered and then attached to the substrate with silver paint. This makes the response time very fast, and the thermocouple does not influence the heat transfer to the substrates. Temperature was measured with a digital thermocouple readout and recorded using a chart-recorder.

Figure 3-1 shows the temperature rise as a function of time of irradiation for several laser currents. The temperature is accurately fitted by the following heat transfer model (Ref. Appendix A):

$$\begin{aligned}\Delta T(t) &= \frac{\varepsilon P}{hA_0} \left[1 - \exp\left(-\frac{h}{c_p \rho d} t\right) \right] \\ &= \Delta T_{\max} (1 - e^{-C_0 t}),\end{aligned}$$

where

$$\Delta T_{\max} \equiv \Delta T(t = \infty) = \frac{\varepsilon P}{hA_0},$$

ε is the total efficiency of the incident laser light (the ratio of the power absorbed by a

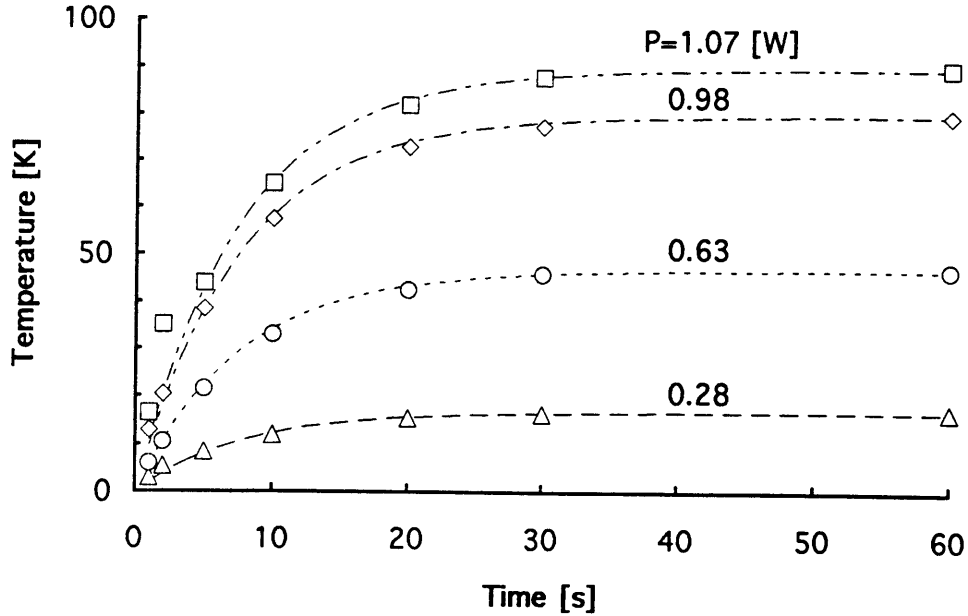


Figure 3-1: Temperature rise during the laser irradiation. Unfilled squares, diamonds, circles, and triangles are temperatures measured with a thermocouple when the laser output powers are 1.07, 0.948, 0.63, and 0.28 W, respectively. Each line is the calculated temperature at the corresponding output power.

substrate to the output power at the output window of the laser, Ref. Appendix B), P is the output power, h is the heat transfer coefficient, A_0 , c_p , ρ , and d are the surface area, heat capacity, density, and thickness of the substrate, respectively, and C_0 is a time constant. AC_0 value of 0.131 s^{-1} is obtained from figure 3-2, which shows the dimensionless temperature

$$\Theta \equiv \frac{\Delta T}{\frac{\varepsilon P}{hA_0}} = 1 - e^{-C_0 t}$$

as a function of time when $P=0.28, 0.63, 0.98, 1.07 \text{ [W]}$. It should be noted that the temperature reaches 90 % of its maximum in 20 s in any case. ΔT_{max} is extracted from the experimental data when the substrate temperature is saturated after 60 s.

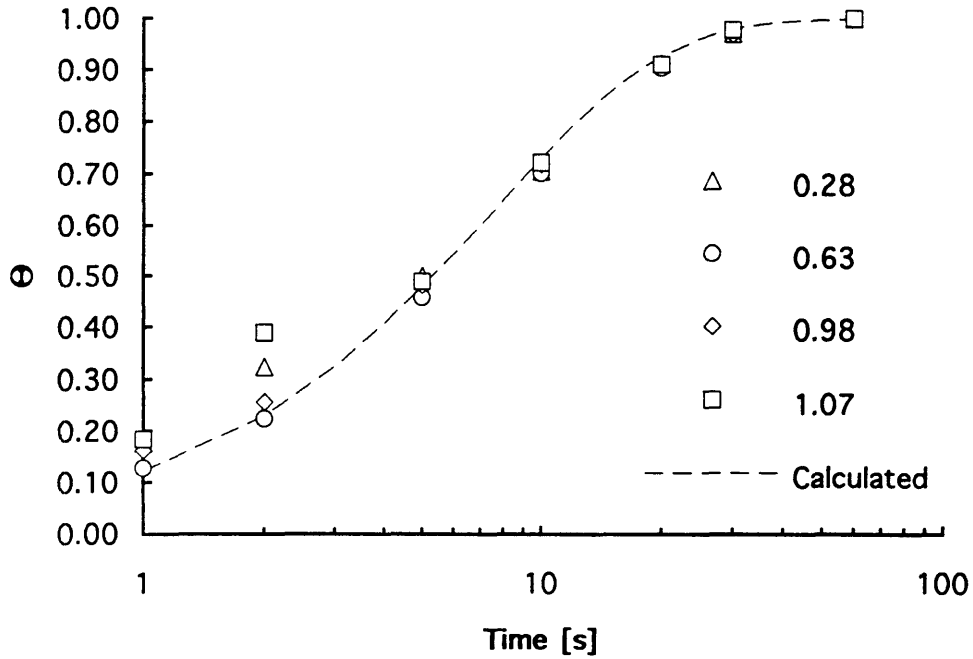


Figure 3-2: Dimensionless temperature as a function of time. The dashed line was fit to the measured values.

3-2 Yield and Growth Rate

Yield and growth rate results are shown in figure 3-3 as a function of laser power. It should be noted that this yield is calculated assuming pure copper lines and that this yield is the *net yield*, or the difference between the decomposition yield and the sputtered yield. Since there is no absorption by the Cu(hfac)TMVS at this wavelength, the variations in the growth rate are due to the changes in the substrate temperature. The small decline in deposition yield in the lower laser power regime may be explained by an increased density of atoms in the deposited films when temperatures are slightly higher than room temperature. This result agrees with the previous study by Della Ratta when the entire substrate was heated up to 120 °C by a resistance heater in the substrate holder[19].

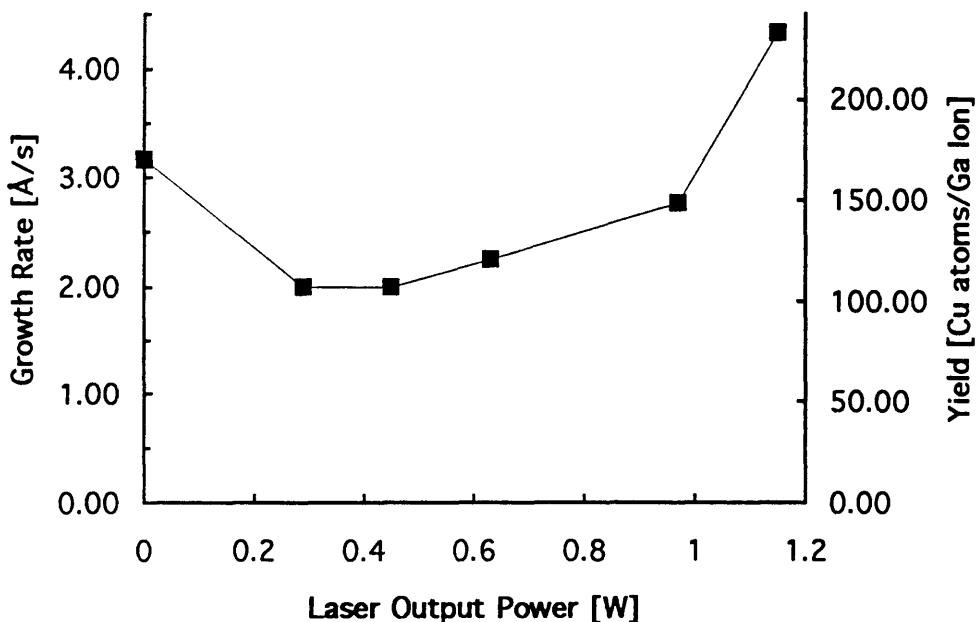


Figure 3-3: Yield and growth rate as a function of laser power. The yield was calculated assuming a rectangular cross-section and using the bulk copper density.

At higher power, the yield is significantly increased. Two explanations were given in the previous study: (a) $\text{Cu}(\text{hfac})\text{TMVS}$ may be dissociated pyrolytically, and (b) the byproduct desorption rate would increase at higher temperature[19]. The first reason is not likely to explain this case since the deposition outside the ion beam is insignificant; in other words, the amount of thermally decomposed copper is not comparable to that from ion-induced decomposition. The second explanation is plausible if the byproducts do not directly enter the gas phase and the desorption process is rate limiting. An alternate explanation takes into account the synergetic effect of ion irradiation and heating. This is schematically shown in figure 3-4. In this model, it is assumed that the rate limiting step in the entire reaction is the process by which a radical $\text{Cu}(\text{hfac})\text{TMVS}^*$ is made. An adsorbed copper precursor is given the energy which is below the threshold value for decomposition by an energetic surface atom (ESA) in collision cascades, and it

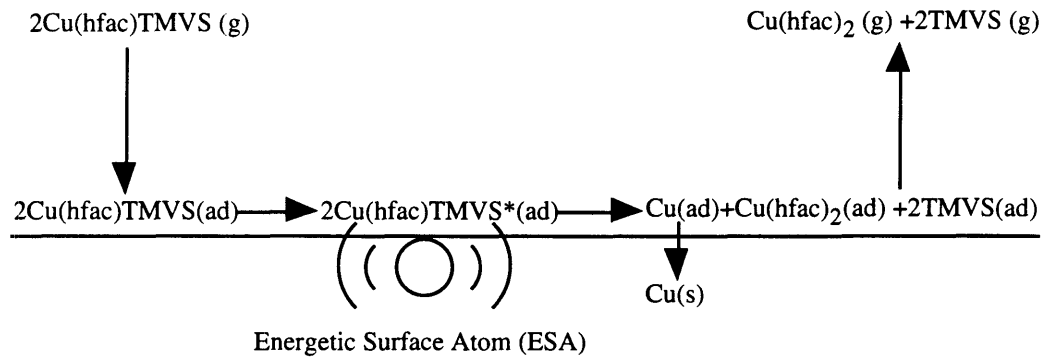


Figure 3-4: Schematic of focused-ion-beam-induced decomposition process of Cu(hfac)TMVS.

becomes a radical. This radical is not stable and is easier to decompose on a substrate that is slightly above room temperature, but below a temperature that causes significant thermal decomposition. Further study is necessary to understand this phenomenon.

3-3 Resistivity

Figure 3-5 shows the resistivity as a function of laser power. At the highest laser power 1.15 W, the resistivity is about $3 \mu\Omega\text{-cm}$ (the bulk copper value is $1.7 \mu\Omega\text{-cm}$). As mentioned before, the effect of laser irradiation is considered to be solely pyrolytic. The resistivities are shown in figure 3-6 as a function of the estimated temperature discussed above. The results from the previous study by Della Ratta are also shown for comparison[19]. In the previous study, the substrate was heated by a resistance-heated substrate holder, and the films were deposited at a local precursor pressure of 1.5 mtorr at an average ion current density of $20 \mu\text{A}/\text{cm}^2$ using 35 keV Ga ions. It can be seen from the figure that both results agree with each other very well even though the deposition conditions were quite different. It implies that the substrate temperature is the most influential growth condition in determining the resistivity of deposited copper films. It is

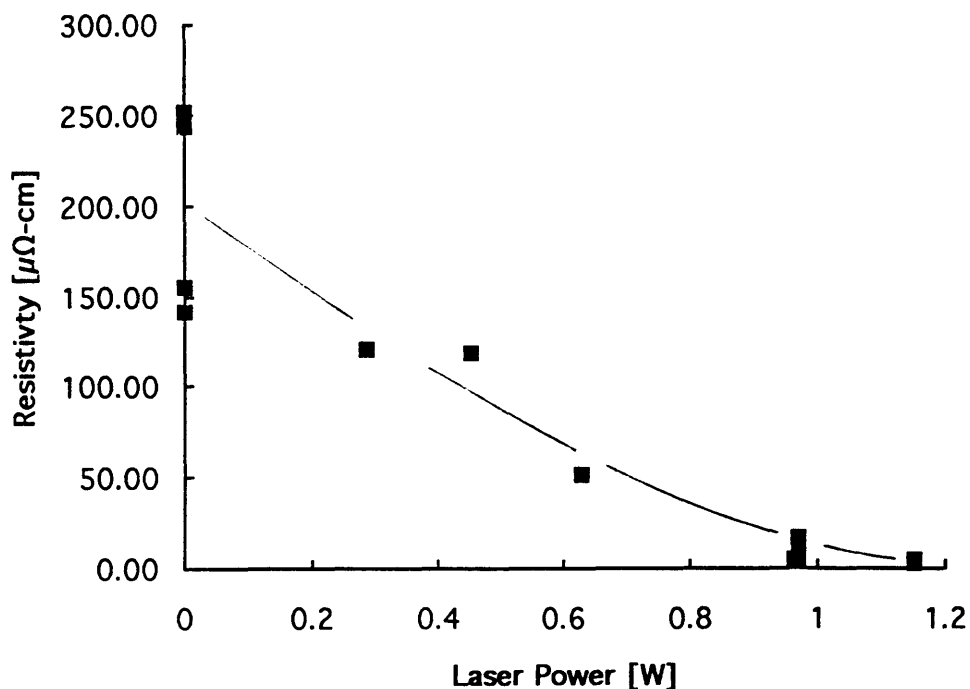


Figure 3-5: Resistivity as a function of laser power. The smallest resistivity of 3 $\mu\Omega$ -cm has been achieved at laser power of 1.15 W.

also seen from the figure that the effect of laser irradiation is solely pyrolytic, as predicted, rather than photolytic.

In the previous study, it had been shown from Auger Electron Spectroscopy that the relative fraction of the copper content increases with increasing deposition temperature. This trend was also observed in gold deposition from dimethyl gold hexafluoro-acetyl-acetonate[28]. The reduced fractions of contaminants were attributed to the increased rate of desorption of byproducts, such as $\text{Cu}(\text{hfac})_2$ and TMVS in figure 3-4, at higher deposition temperatures. Since the laser is simply heating the substrate rather than decomposing the precursor photolytically, it is expected that the film deposited at higher laser power contains a larger fraction of copper than a lower power deposit.

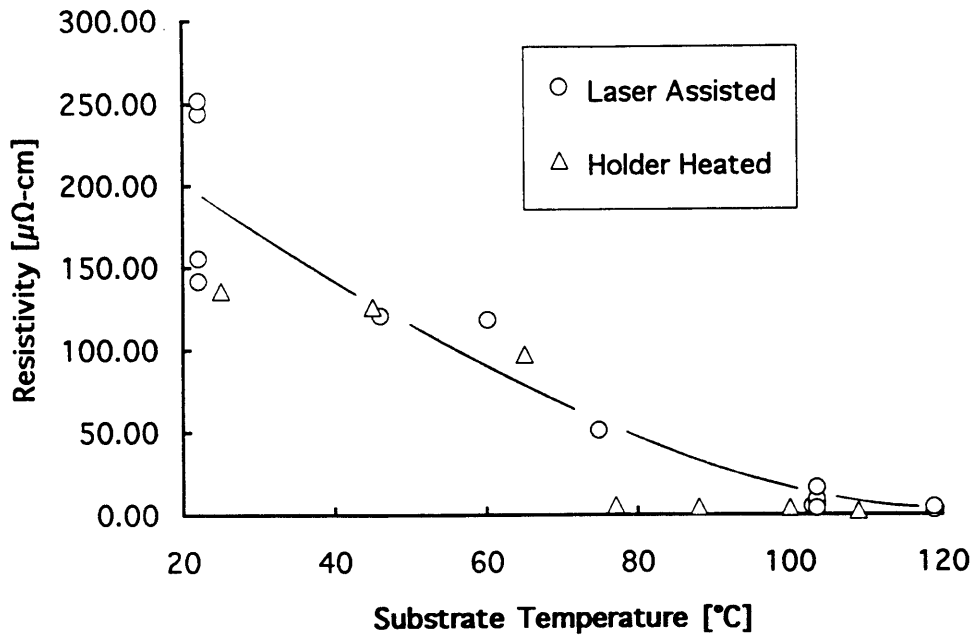


Figure 3-6: Resistivity as a function of estimated substrate temperature. The results from the previous study by Della Ratta are also shown for comparison[19]. In the previous study, the substrate was heated by a resistance-heated substrate holder, and the films were deposited at a local precursor pressure at 1.5 mtorr at an average ion current density of 20 $\mu\text{A}/\text{cm}^2$ using 35 keV Ga ions.

The resistivity is a critical characteristic of the deposited film. A low resistivity shows that the film contains little contaminants such as oxygen and carbon, and consists of relatively large grains which are well connected with each other. The resistance is also significant in practical applications since it strongly influences circuit-delays. Considering circuit repair of VLSIs, the time needed to deposit a line at a certain resistance is an important factor.

The resistance is given by

$$R = \rho \frac{l}{A},$$

where ρ is the resistivity, l is the length, and A is the cross-section area. A is the product

of the width and thickness of the film. The thickness is simply the product of the growth rate and deposition time. The resistance is then expressed in terms of the deposition time as,

$$R = \frac{l \cdot \rho}{wd \cdot t},$$

where w is the width, \dot{d} is the growth rate, and t is the deposition time. Assuming that the growth rate and resistivity are constant, the resistance should be proportional to the inverse deposition time. Figure 3-7 shows the resistance of deposited lines as a function of inverse deposition time. The laser power used to assist in deposition was 1.12 W and the substrate temperature is estimated to be 120 °C. The line width and length are 1.6 and 100 μm , respectively. It can be clearly seen from the figure that this assumption is not correct.

A previous study has shown that the growth rate is constant for ion doses ranging from 1.6×10^{16} to 1.7×10^{17} ions/cm²[24]. These ion doses correspond to 29 s and 309 s of deposition, respectively, for the average current density of 88 $\mu\text{A}/\text{cm}^2$ used in this study. Therefore, the growth rate may be assumed to be constant; that is, the resistivity may not be assumed to be constant. The resistivity can be obtained by using the constant growth rate 4.3 $\text{\AA}/\text{s}$ obtained from figure 3-3,

$$\rho = R \frac{wdt}{l}.$$

Figure 3-8 shows the normalized resistivity, or the ratio of the calculated resistivity to the pure bulk copper value,

$$\Phi \equiv \frac{\rho}{\rho_{Cu}} = \frac{R}{\rho_{Cu}} \frac{wdt}{l},$$

as a function of deposition time. It can be seen from the figure that the resistivity of the lines deposited for short times is much higher than that for long times. This trend may be explained by the connectivity of the grains of the deposited films.

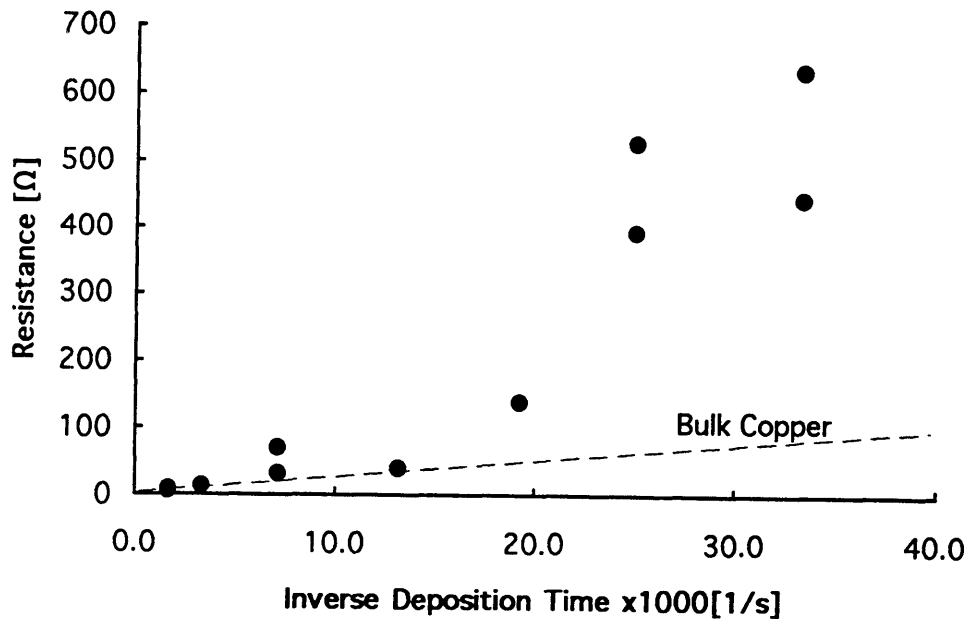


Figure 3-7: The resistance of deposited lines as a function of inverse deposition time. The laser power used was 1.12 W, and the substrate temperature was estimated to be 120 °C. The line width and length are 1.6 and 100 μm, respectively. The dashed line indicates the resistance calculated by taking bulk copper resistivity and a constant growth rate of 4.3 Å/s.

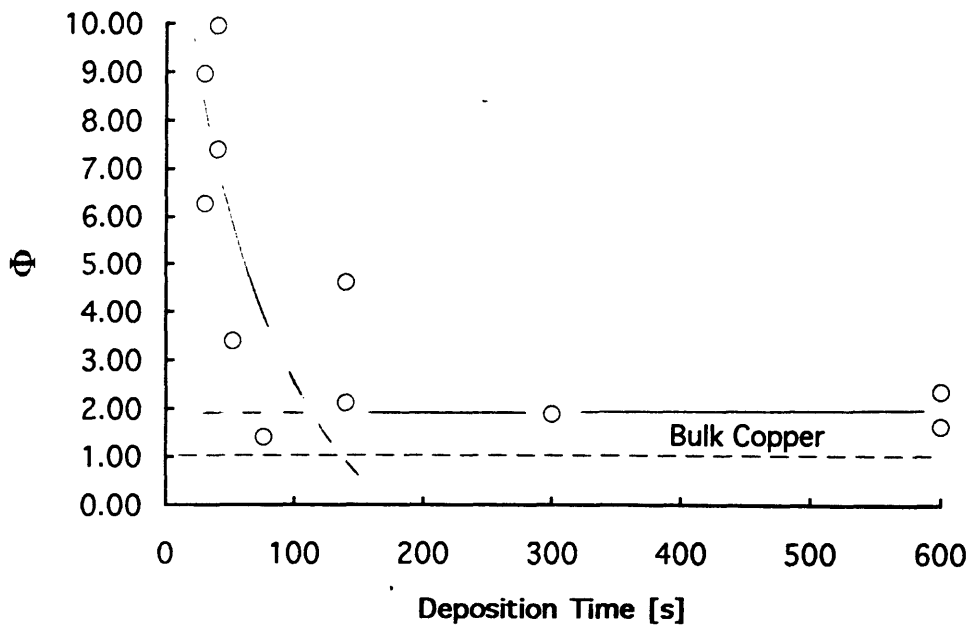


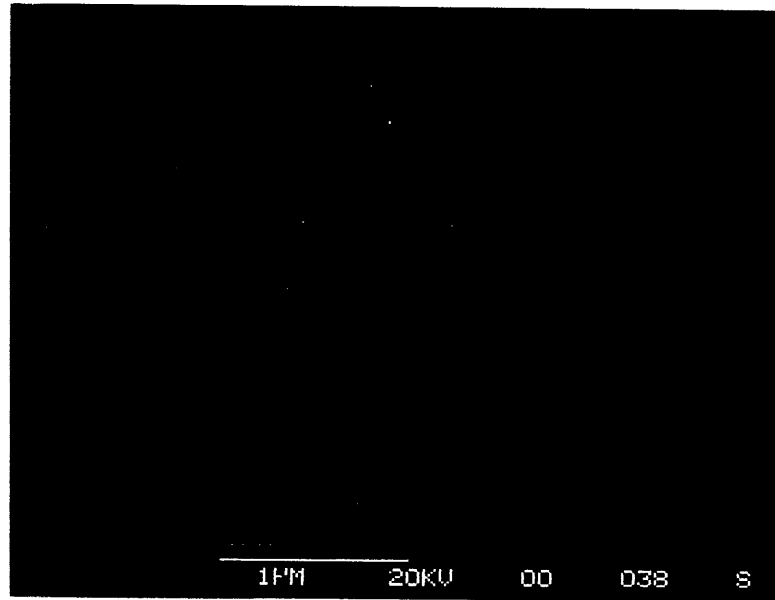
Figure 3-8: The normalized resistivity as a function of deposition time. The resistivity is obtained by using a constant growth rate of 4.3 Å/s

It has been shown from TEM studies of copper deposition by Della Ratta[19] and gold deposition by Dubner[42] that the microstructures consist of continuous metal grains, approximately 1000 Å in size, with little carbon at the grain boundaries at higher deposition temperature. Assuming a constant number of nucleation sites which are located at each crossing of a square grid, and that semi-spherical crystals grow with an isotropic rate, it is estimated that it takes 120 s to become a 1000 Å diameter grain, which is connected to the adjacent grains. This period of time roughly corresponds to the kink in figure 3-9.

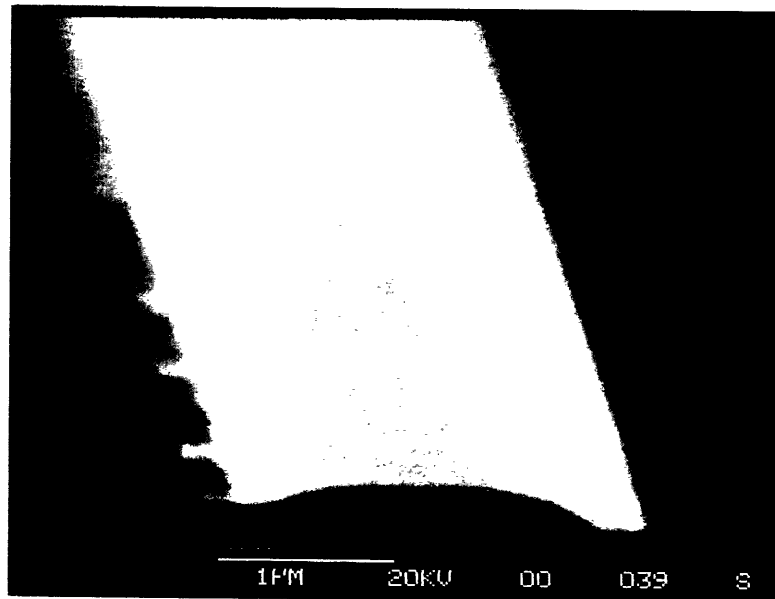
3-4 Microstructure

Figure 3-9 shows the SEM micrographs of a copper film deposited at room temperature without using the laser. The figure shows that the surface of these films is relatively smooth. Thin layers of deposit adjacent to the line are observed from early stages of deposition. It may be attributed to the presence of beam "skirts" as shown in figure 1-5, or sputtered materials from the deposited film. The 1.6 μm line width obtained from the SEM micrographs was much larger than the beam diameter, which is estimated to be 450 Å. Considering the 2500 Å line width previously achieved with this FIB system[19], the incident angle of the ion beam (45 degrees) alone cannot explain this lower resolution.

Figure 3-10 shows an SEM micrograph of a copper line deposited with laser irradiation at 1.0 W. The substrate temperature is estimated to be 110 °C. The surface morphology shows grain-like structures on and along the deposited line. The largest grain size in this structure is roughly 500 Å, which is on the order of the grain size discussed above.



(a)



(b)

Figure 3-9: Scanning electron micrographs of copper lines deposited for (a) 1 minute and (b) 10 minutes without laser irradiation.

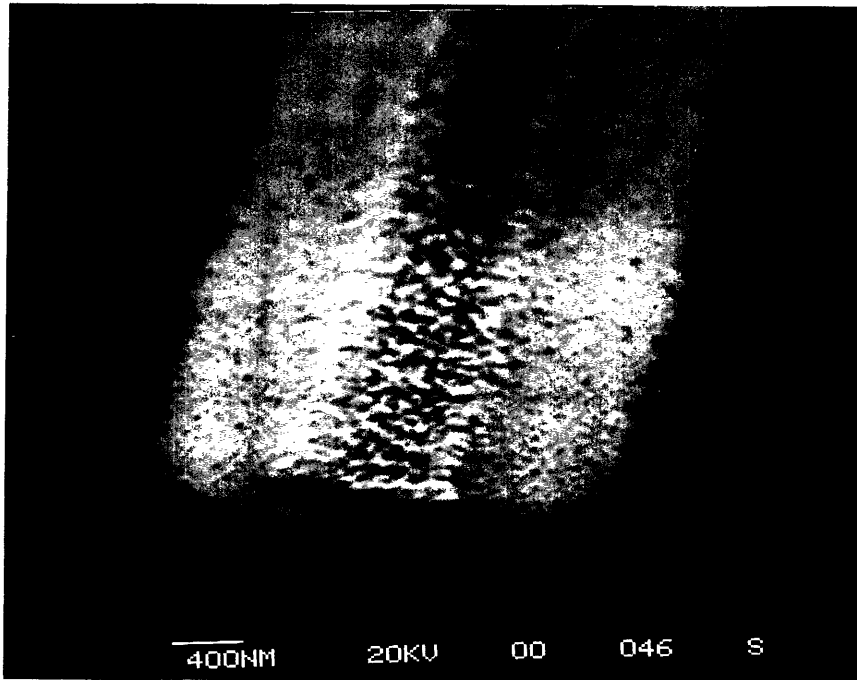


Figure 3-10: A scanning electron micrograph of a copper line deposited for 10 minute with laser irradiation of 1 W. The substrate temperature is estimated to be 110 °C.

It has been demonstrated that higher deposition temperatures yield lower film resistivities[19][27]. However, in conventional heating, the line width of the deposited films was enlarged due to the stage drift in deposition. A local heating source has been proposed to solve this problem.

Figure 3-11 shows the line width and aspect ratio defined as

$$\beta = \frac{d}{w},$$

where d and w are the height and width of lines. The lines deposited with higher laser power become slightly wider than those deposited without using the laser. The aspect ratio becomes smaller, or the lines become flat, when deposited at higher laser power. The stage drift, which contributed to the widening of the deposited lines in the previous

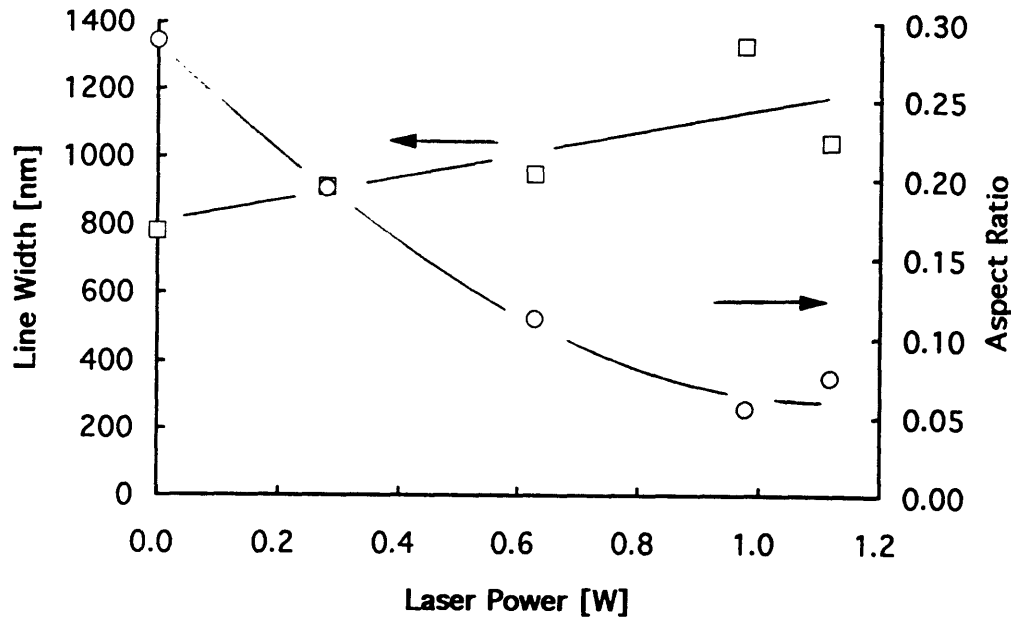


Figure 3-11: The line width and aspect ratio of the deposited copper lines as a function of laser output power. The aspect ratio is obtained by dividing the line height by line width.

studies, has not been observed here. It was not feasible in this FIB system to directly compare the line resolutions between the laser heating and the conventional resistance heating. However, the stage drift in laser heating is thought to be considerably smaller than that in resistance heating, since the heat flux to the sample stage in laser heating is only up to 0.4 W (Ref. Appendix B), which is significantly smaller than that for conventional resistance heating, and the temperature change of the stage is negligible.

3-5 Summary

In this chapter, experimental results of heating, growth rate, resistivity, and microstructure have been delineated for laser-assisted focused-ion-beam-induced CVD. The substrate temperature is raised up to 120 °C at 1W of laser power. The growth rate ranges from 2.0 to 4.3 Å/s. The dependency of the resistivity on the estimated substrate temperature showed that laser irradiation is effective pyrolytically rather than photolytically. The lowest resistivity, 3 μΩ-cm, close to the bulk copper value, 1.7 μΩ-cm, has been achieved in lines deposited at 1.1 W of laser power. When deposited at high temperature, the film becomes coarse and granular, and the aspect ratio becomes smaller due to the increased line width. Since the heat flux to the sample stage is significantly smaller than that for conventional resistance heating, the stage drift in laser heating is thought to be considerably smaller than that in resistance heating.

4. Summary and Future Work

4-1 Summary

In this study, it has been demonstrated that a semiconductor laser is an effective tool for reducing the resistivity of focused-ion-beam-induced deposited copper films. This provides an alternative to heating of the entire substrate which causes thermal drift and reduces the resolution. The output power of the laser (wavelength of 977 nm) is easily controlled by monitoring the laser current, and it ranges continuously from 0 to 1.2 W at a current of 0.6 to 2.5 A, respectively. The laser was focused onto thermally grown SiO₂ on an Si substrate, and its spot area is estimated to be 5.90×10^{-5} cm², which gives a maximum intensity of 2.0×10^4 W/cm². Even though the laser beam was focused onto a small area, the Si substrate was uniformly heated due to the high thermal diffusivity of silicon and the small sample size, $5 \times 10 \times 0.38$ mm³. However, considering x-ray mask repair applications, this optical setting could give sufficient light intensity to locally heat a glass substrate since the thermal diffusivity of an SiO₂-based glass is typically two orders of magnitude smaller than that of silicon. It is also possible to achieve a smaller spot size by using a more complicated optical system, so that only a local area of a silicon substrate will be heated.

The organometallic complex used in this study was copper hexafluoro-acetyl acetate trimethyl-vinylsilane, which has no absorption in the gas phase at 977 nm. As a result, the dependencies of the growth rate and resistivity of films deposited using this laser on the estimated substrate temperature are in good agreement with those deposited by using a conventional resistance heating. The growth rate ranges from 2.0 to 4.3 Å/s, depending on the laser power. A small decline in the growth rate in the relatively low laser power regime was observed. This agrees with the smaller yield found in a previous study around the substrate temperature of 45 °C[19]. At higher laser powers, the growth

rate is significantly increased. The lowest resistivity, $3 \mu\Omega\text{-cm}$, close to the bulk copper value, $1.7 \mu\Omega\text{-cm}$, has been achieved when deposited at laser power of 1.1 W. At this laser power, the substrate temperature is estimated to be 120°C . When deposited at high temperature, the deposited film become coarse and granular. The grain size is estimated to be 500 to 1000 \AA using an SEM, which is consistent with TEM in previous studies[19][42].

The smallest line width $0.8 \mu\text{m}$ has been achieved when deposited without using the laser. The deposited lines become slightly wider for higher laser powers, causing the aspect ratio to become smaller. It was not feasible in this FIB system to directly compare the line resolutions between laser heating and the conventional resistance heating. However, the stage drift in laser heating is thought to be considerably smaller than that in resistance heating, since the heat flux to the sample stage in laser heating is only up to 0.4 W (Ref. Appendix B), which is significantly smaller than that for conventional resistance heating, and the temperature change of the stage is negligible.

4-2 Future Work

Although it was demonstrated that a semiconductor laser and its optical arrangement is useful in reducing the resistivity of films deposited using a FIB, further refinements, such as adding a function to monitor the laser spot with an infrared camera and reducing the spot size by using a more sophisticated optical system, are necessary for practical applications in x-ray mask repairs or circuit repairs in very large scale IC's. A more thorough study is necessary to understand the time dependent resistivity at early stages of deposition. A more detailed study of desorption mechanism will be useful for understanding the lower resistivity and higher growth rate observed when films are deposited at higher deposition temperature. Use of some form of radiation will provide an alternative to heating the entire substrate, reducing spatial resolution and positioning problems associated with thermally induced stage drift.

Appendix A: Temperature Calculation

Substrate temperature is a critical parameter in FIB deposition. The temperature rise during laser irradiation has been measured using a thermocouple, and calculated using classical heat transfer methods. Two models were considered: an infinite sheet model and a heat transfer model. In the first model, an infinitely large two-dimensional solid irradiated by a spot heat source is considered. The other model assumes the entire substrate is uniformly heated, and the heat is transported to the substrate holder.

A-1 Infinite Sheet Model

In this model, it is assumed that the total laser power is focused evenly in a circular area on the surface of an infinite sheet as shown in figure A-1. This simplifies the solution and its result is equal to the exact solution for the decaying Gaussian beam model[45], after a reasonable time period (1 ms for Si substrate with 40 μm beam radius)[46], which is much shorter than typical deposition time period, 600s. In general, the conduction of heat in a three dimensional solid is given by the solution to the differential equation,

$$\rho C \frac{\partial T}{\partial t} = \frac{\partial}{\partial x} \left(K \frac{\partial T}{\partial x} \right) + \frac{\partial}{\partial y} \left(K \frac{\partial T}{\partial y} \right) + \frac{\partial}{\partial z} \left(K \frac{\partial T}{\partial z} \right) + A(x, y, z, t),$$

where the thermal conductivity K , the density ρ , and the specific heat C are dependent on both temperature and position, and heat is supplied to the solid at a rate of $A(x, y, z, t)$.

Since the temperature range is small (20-120 $^{\circ}\text{C}$), thermal properties may be regarded as constants. Assuming the Si wafer is homogeneous and isotropic, the above equation reduces to

$$\nabla^2 T - \frac{1}{\kappa} \frac{\partial T}{\partial t} = -\frac{A(x, y, z, t)}{K},$$

where $\kappa = K/\rho C$ is the thermal diffusivity.

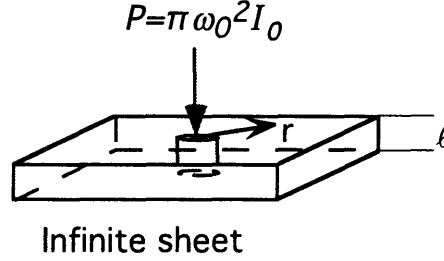


Figure A-1: Schematic of the infinite sheet model with a cylindrical heat source. The total power P is focused to a circular area (πw_0^2 on the surface). w_0 is the beam diameter and I_0 is the average beam intensity. Temperature was calculated as a function of radial distance r from the beam center.

Further simplification is possible if the total power P is focused to a circular area πw_0^2 on the surface of an infinite sheet as shown in figure A-1. The absorbed radiation is assumed to uniformly heat a circular cylinder of area πw_0^2 and height ℓ .

This cylinder is assumed to have infinite thermal conductivity so that the absorbed power is dissipated uniformly into the surrounding sheet with intensity

$$F = \frac{\varepsilon P}{2\pi w \ell},$$

where ε is the fraction of the total power absorbed by the substrate (Ref. Appendix B).

In this case, the temperature outside the cylindrical area as a function of radial distance r from the beam center is given by

$$T(r, t) = \frac{P\varepsilon}{4\pi K \ell} \left[\ln\left(\frac{4\kappa t}{Cr^2}\right) + \frac{\omega_0^2}{2\kappa t} \ln\left(\frac{4\kappa t}{Cr^2}\right) + \frac{1}{4\kappa t} \left(\omega_0^2 + r^2 - 2\omega_0^2 \ln\frac{\omega}{r} \right) \right],$$

where C is a constant, 1.781, if the condition $w^2 \ll \kappa t$ is satisfied[46]. The temperature inside the area is given by

$$T(r, t) = \frac{P\varepsilon}{4\pi K \ell} \left[\ln\left(\frac{4\kappa t}{C\omega_0^2}\right) + \frac{\omega_0^2}{2\kappa t} \ln\left(\frac{4\kappa t}{C\omega_0^2}\right) + \frac{\omega_0^2}{2\kappa t} \right].$$

Figure A-2 shows the temperature rise at the center of the laser spot as a function of time when the 1W laser is focused to the spot of diameter 43 μm .

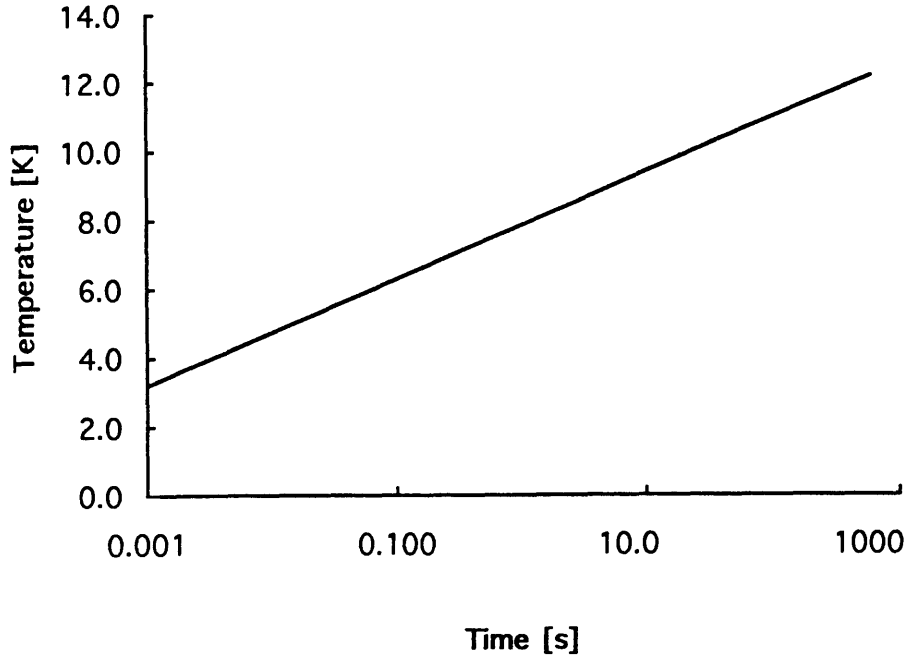


Figure A-2: Temperature rise at the center of the laser spot calculated using an infinite sheet model as a function of time when the 1 W laser is focused to the spot of diameter $43 \mu\text{m}$. The constants ε , κ , K , and ℓ for Si wafers used in this study are 0.48, $0.9 \text{ cm}^2/\text{s}$, 1.48 W/cm-K , and $380 \mu\text{m}$, respectively.

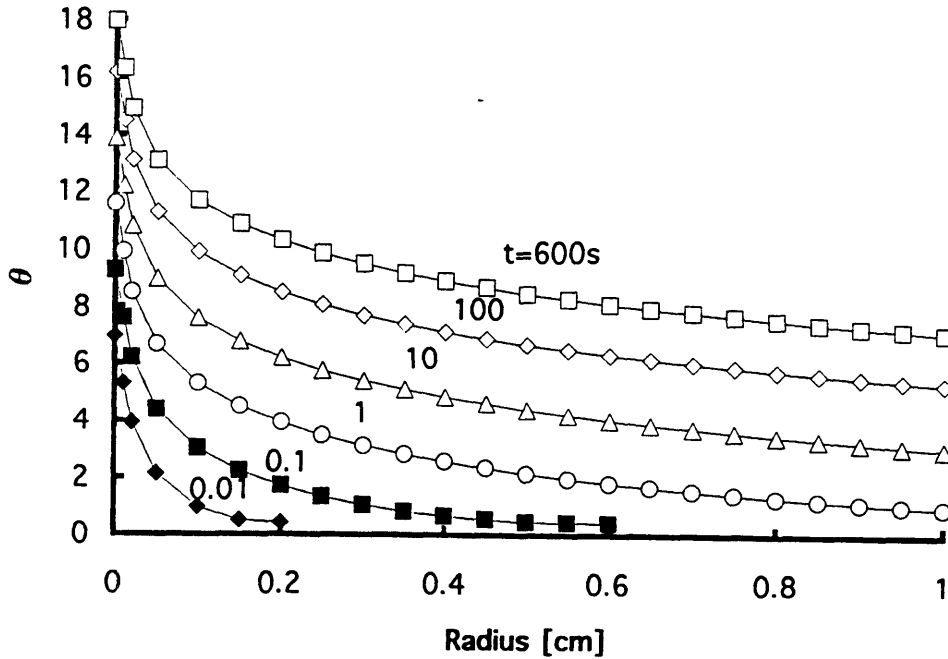


Figure A-3: Dimensionless temperature profile calculated using an infinite sheet model after time t s of the laser irradiation.

The constants ε , κ , K , and ℓ for Si wafers used in this study are 0.48, 0.9 cm²/s, 1.48 W/cm-K, and 380 μ m, respectively. The maximum temperature rise during a typical deposition (600 s) is 12.2 K, which is significantly lower than the measured temperature.

Figure A-3 shows the dimensionless temperature

$$\theta \equiv \frac{4\pi K l}{P \varepsilon},$$

outside the cylindrical area as a function of radial distance r . Since Si has a relatively large thermal diffusivity, a fraction of the heat flux reaches the edge of sample ($r=0.25$ mm) in less than 0.01 s. The model assumes an infinite sheet; therefore, the heat dissipates rapidly. However, in these experiments, the heat does not dissipate as described above but raises the temperature of a finite substrate substantially.

A-2 Heat Transfer Model

The other model assumes that the entire substrate is uniformly heated, and the heat is transported to the substrate holder as shown in figure A-4. This heat flux is assumed to be linearly proportional to the difference between the substrate temperature T and the constant holder temperature T_0 , and its proportionality is

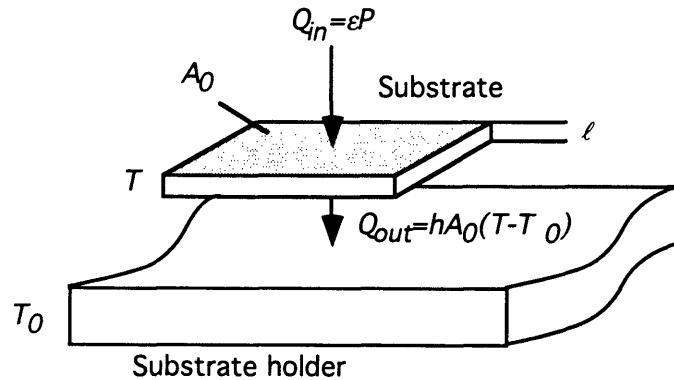


Figure A-4: Schematic of heat transfer model. Heat flux from the substrate to its holder is assumed to be proportional to their temperature difference.

given by a heat transfer coefficient h . From the heat balance, the temperature change of the substrate is expressed by

$$c_p \rho A_0 l \frac{dT}{dt} = Q_{in} - Q_{out},$$

where c_p is the specific heat, ρ is the density, A_0 is the surface area, l is the thickness of the substrate, and

$$Q_{in} = \varepsilon P,$$

where ε is the fraction of total laser output absorbed by the substrate, and

$$Q_{out} = h(T - T_0)A_0.$$

The substrate temperature is given by solving this simple differential equation:

$$T = T_0 + \frac{\varepsilon P}{hA_0} \left[1 - \exp\left(-\frac{h}{c_p \rho l} t\right) \right].$$

The unknown constants in this equation are h and ε . h is obtained by measuring the substrate temperature and plotting the dimensionless temperature

$$\Theta \equiv \frac{\Delta T}{\frac{\varepsilon P}{hA_0}} = 1 - \exp\left(-\frac{h}{c_p \rho l} t\right),$$

where

$$\Delta T = T - T_0.$$

As shown in figure 3-2, the calculated temperature can be fitted very well to the measured value with $h=8.23 \times 10^{-3}$ W/cm²-K. ε is obtained from the maximum temperature rise

$$\Delta T_{\max} \equiv \Delta T(t = \infty) = \frac{\varepsilon P}{hA_0}.$$

In practice, the temperature reaches a maximum after 60 s as shown in figure 3-1. From the figure, when a power $P=1.07$ W is irradiated on a 0.5 cm² substrate, $\Delta T_{\max}=90$ K, and this gives an ε of 0.35. This value agrees reasonably well with the calculated value of 0.43 (Ref. Appendix B). The smaller value can be attributed to the smaller numerical

aperture (NA) of the collimator, which causes a loss when collecting the outer boundaries of the laser beam.

Appendix B: Total Efficiency in Laser Beam Irradiation

In this study, a semiconductor laser with a 977 nm wavelength has been used to heat substrates in order to reduce the resistivity of deposited copper lines. It has been shown that the resistivity is strongly dependent on the laser output power. In Appendix A, the substrate temperature rises were calculated with two models, and it was found that the temperature rises calculated with the heat transfer model are good in agreement with the measured values. The temperature rise is given by

$$\Delta T = \frac{\epsilon P}{hA_0} \left[1 - \exp\left(-\frac{h}{c_p \rho l} t\right) \right],$$

where ϵ is the total efficiency in laser beam irradiation, P is the laser output power, h is the heat transfer coefficient, t is the duration of laser irradiation, and A_0 , C_p , ρ , and ℓ are the surface area, specific heat, density, and thickness of the substrate, respectively. In this equation, ϵ and h were experimentally obtained in this study, and they are 0.35 and $8.23 \times 10^{-3} \text{ W/cm}^2\text{-K}$, respectively. In this appendix, ϵ will be obtained by considering

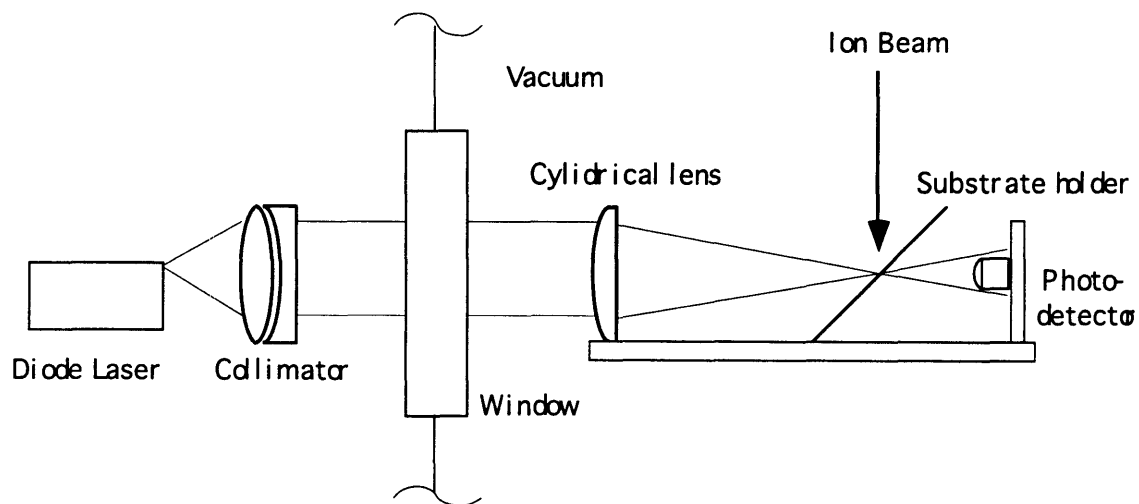


Figure B-1: A schematic of the semiconductor laser and its focusing optics.

transmittance and reflectance of the collimator, window, cylindrical lens, and substrate shown in figure B-1.

B-1 General Theory of Optics

The intensity of the light decaying exponentially in passing through a material is given by

$$I = I_0 e^{-\alpha z},$$

where I_0 is the intensity at the surface, α is the absorption coefficient, and z is the depth from the surface. The relation between α and the refractive index is given by

$$\alpha = \frac{4\pi k}{\lambda},$$

where k is the extinction coefficient or imaginary part of the complex refractive index

$$m = n - ik,$$

while λ is the wavelength of incident light. n is the index of refraction, or the real part of the complex refractive index; it is the ratio between the speed of light in vacuum (c) and that in the medium (v), $n = c/v$.

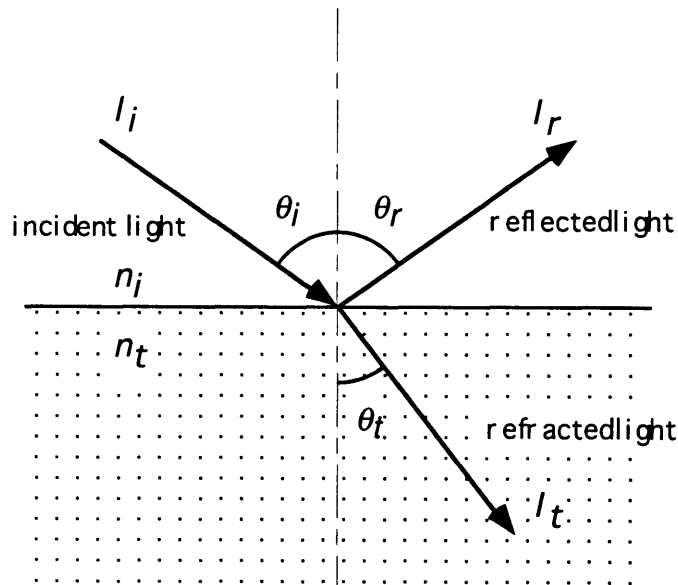


Figure B-2: Reflection and transmission of plane wave.

In general , light is incident on the smooth medium at an angle of θ_i as shown in figure B-2. The reflectance R of an incident light is defined as

$$R \equiv \frac{I_r \cos \theta_r}{I_i \cos \theta_i} = \frac{I_r}{I_i},$$

where I is the average power crossing a unit area, θ is the angle between the light and the normal to the interface, subscript r and i are reflected and incident light, respectively.

The transmittance T is defined as

$$T \equiv \frac{I_t \cos \theta_t}{I_i \cos \theta_i},$$

where subscript t is transmitted light. The relation between θ_i and θ_t is given by Snell's law,

$$n_i \sin \theta_i = n_t \sin \theta_t,$$

Assume two cases; (1) the electric field \mathbf{E} is perpendicular to the plane of incidence as shown in figure B-3(a), and (2) the electric field is parallel to the plane as in figure B-3(b). When \mathbf{E} is perpendicular to the plane of incidence and the magnetic field \mathbf{B} is parallel to it, the ratio r of the amplitude of the electric field of incident light to that of reflected light is

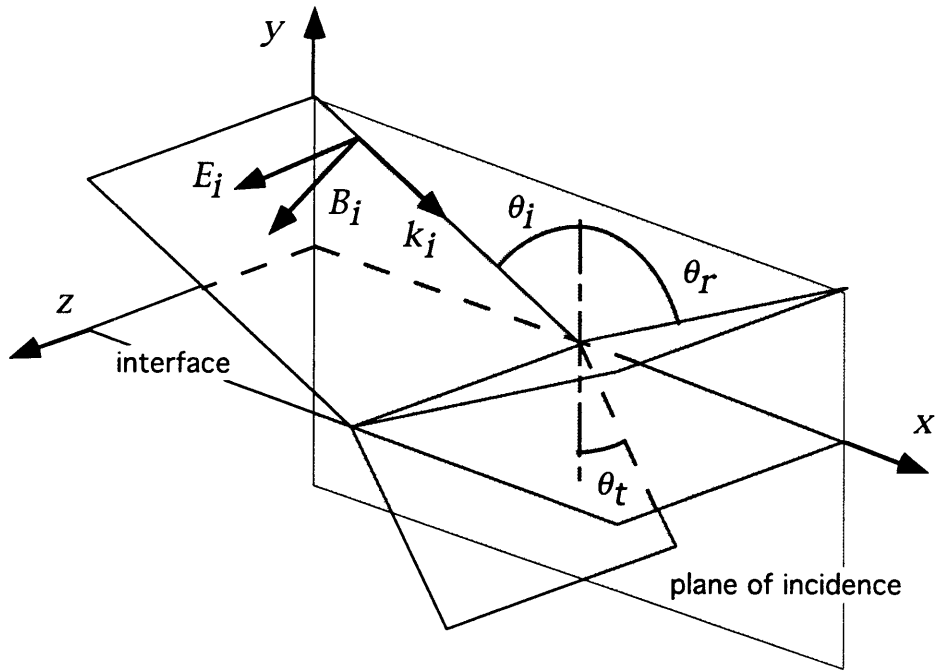
$$r_{\perp} \equiv \left(\frac{E_{0r}}{E_{0i}} \right)_{\perp} = \frac{\frac{n_i}{\mu_i} \cos \theta_i - \frac{n_t}{\mu_t} \cos \theta_t}{\frac{n_i}{\mu_i} \cos \theta_i + \frac{n_t}{\mu_t} \cos \theta_t},$$

where μ is the permeability of the medium [47]. The ratio t of the amplitude of the electric field of incident light to that of transmitted light is

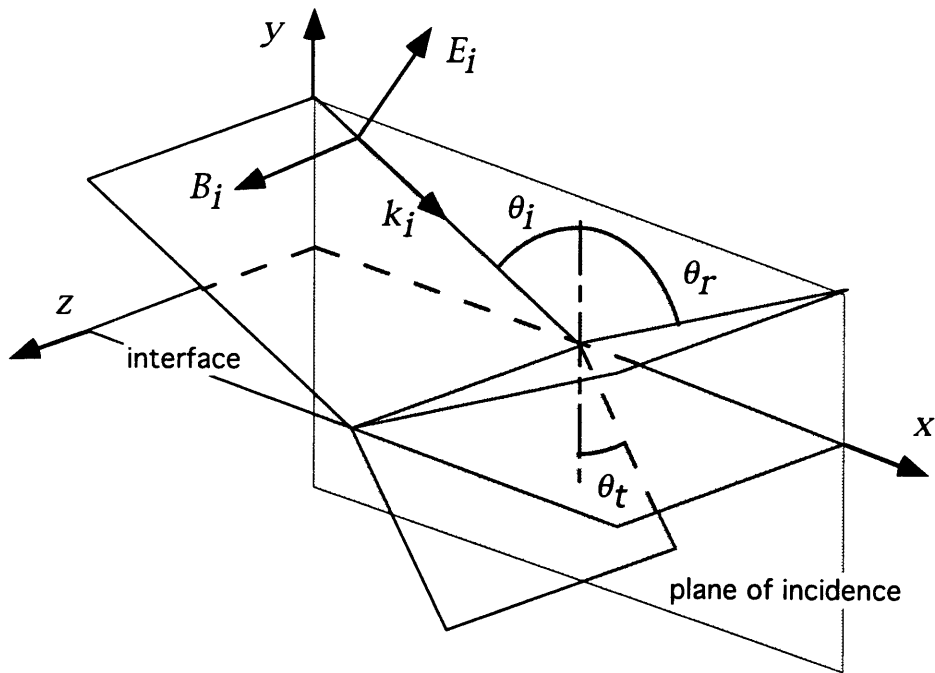
$$t_{\perp} \equiv \left(\frac{E_{0t}}{E_{0i}} \right)_{\perp} = \frac{2 \frac{n_i}{\mu_i} \cos \theta_i}{\frac{n_i}{\mu_i} \cos \theta_i + \frac{n_t}{\mu_t} \cos \theta_t}.$$

Considering a diamagnetic or paramagnetic material, its permeability is very close to that of vacuum and air, $\mu_i \approx \mu_t \approx \mu_0$. In this case, these equations reduce to

$$r_{\perp} \equiv \left(\frac{E_{0r}}{E_{0i}} \right)_{\perp} = \frac{n_i \cos \theta_i - n_t \cos \theta_t}{n_i \cos \theta_i + n_t \cos \theta_t},$$



(a)



(b)

Figure B-3: An incoming wave whose electric field is (a) normal to the plane of incidence and (b) in the plane of incidence.

and

$$t_{\perp} \equiv \left(\frac{E_{0t}}{E_{0i}} \right)_{\perp} \approx \frac{2n_i \cos \theta_i}{n_i \cos \theta_i + n_t \cos \theta_t}.$$

When \mathbf{E} is parallel to the plane of incidence and the magnetic field \mathbf{B} is normal to it, the ratio r of the amplitude of \mathbf{E} of incident light to that of reflected light is

$$r_{//} \equiv \left(\frac{E_{0r}}{E_{0i}} \right)_{//} = \frac{\frac{n_t}{\mu_t} \cos \theta_i - \frac{n_i}{\mu_i} \cos \theta_t}{\frac{n_t}{\mu_t} \cos \theta_i + \frac{n_i}{\mu_i} \cos \theta_t}.$$

Similarly, the ratio t of the amplitude of \mathbf{E} of incident light to that of transmitted light is

$$t_{//} \equiv \left(\frac{E_{0t}}{E_{0i}} \right)_{//} = \frac{2 \frac{n_i}{\mu_i} \cos \theta_i}{\frac{n_t}{\mu_t} \cos \theta_i + \frac{n_i}{\mu_i} \cos \theta_t}.$$

Assuming $\mu_i \approx \mu_t \approx \mu_0$, these equations are

$$r_{//} \equiv \left(\frac{E_{0r}}{E_{0i}} \right)_{//} \approx \frac{n_t \cos \theta_i - n_i \cos \theta_t}{n_t \cos \theta_i + n_i \cos \theta_t},$$

and

$$t_{//} \equiv \left(\frac{E_{0t}}{E_{0i}} \right)_{//} \approx \frac{2n_i \cos \theta_i}{n_t \cos \theta_i + n_i \cos \theta_t}.$$

Since the radiant flux density in vacuum is

$$I = \frac{c^2 \epsilon_0}{2} E_0^2,$$

where c is the speed of light, ϵ_0 is permittivity in vacuum, the reflectance is given by[47]

$$R \equiv \frac{I_r \cos \theta_r}{I_i \cos \theta_i} = \frac{I_r}{I_i} = \left(\frac{E_{0r}}{E_{0i}} \right)^2 = r^2.$$

The transmittance is similarly given by[47]

$$T \equiv \frac{I_t \cos \theta_t}{I_i \cos \theta_i} = \left(\frac{n_t \cos \theta_t}{n_i \cos \theta_i} \right) t^2.$$

In the case of normal incidence from vacuum or air to the medium, the reflectivity is

$$R_0 = \frac{(n-1)^2 + k^2}{(n+1)^2 + k^2}.$$

B-2 Calculation of the Net Efficiency

The window and cylindrical lens shown in figure B-1 are made of fused silica and have vacuum(or air)/silica interfaces. As discussed above, the reflectivity at each interface is

$$R_0 = \frac{(n-1)^2 + k^2}{(n+1)^2 + k^2} \cong 3.37 \times 10^{-2},$$

since $n=1.45$ and $k=6.48 \times 10^{-7}$ for silica at a 977 nm wavelength[48]. The absorption coefficient for silica is $8.34 \times 10^{-2} \text{ cm}^{-1}$ at this wavelength. The ratio between the intensity of light entering the medium to that escaping it is given by

$$\zeta \equiv \frac{I(z)}{I_0} = e^{-\alpha z}.$$

Since the thicknesses of the window and the lens are 0.44 and 0.53 mm, respectively, the corresponding ratios are 0.964 and 0.957. The net transmittance, the ratio between the intensity of the light before entering the medium and that after escaping from the medium, is obtained by

$$\eta = (1 - R_0)^2 \zeta,$$

since there are two interfaces in each medium. The resulting net transmittances for the window η_w and that for the lens η_ℓ are 0.90 and 0.89, respectively. The net transmittance of the collimator η_c is specified (0.95).

Silicon has a relatively small absorption coefficient of $1.8 \times 10^2 \text{ cm}^{-1}$ at a 977 nm wavelength[49]. Since the typical thickness of the silicon wafer used in this experiment is 380 μm , more than 99.9 % of the incident power is absorbed within the wafer. The extinction coefficient k of Si at 0.977 μm is then calculated;

$$k = \frac{\alpha \lambda}{4\pi} = 1.4 \times 10^{-3}.$$

The complex refractive index of Si at this wavelength is 3.56 [49]

In this study, the laser was incident on the Si substrate at 45° , and the laser was operated at TE mode where the electric field is parallel to the junction plane of the laser.

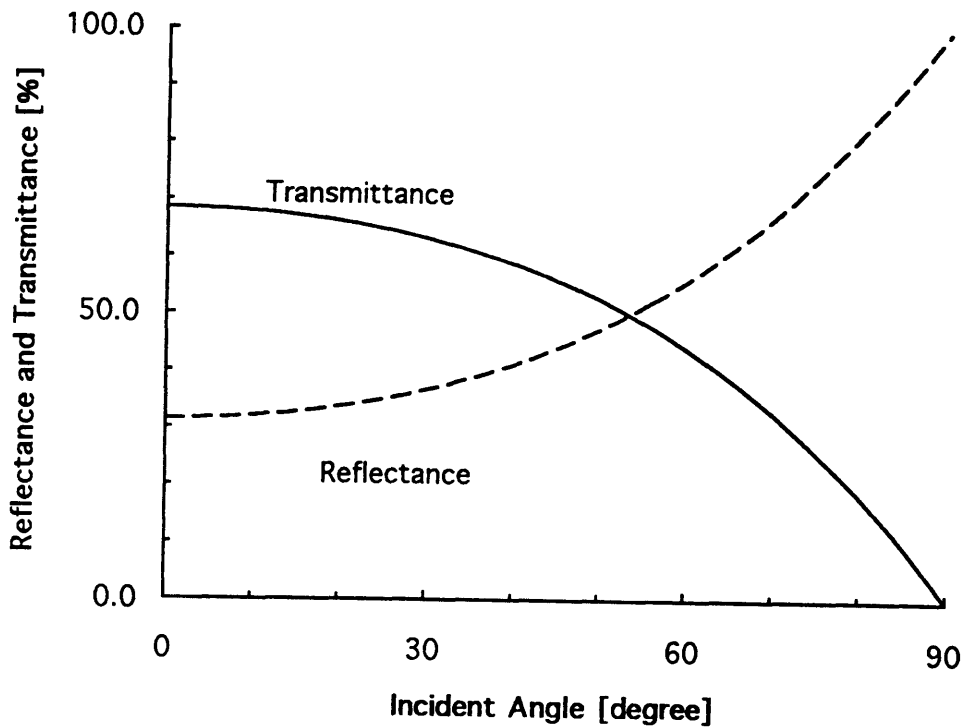


Figure B-4: Reflectance and transmittance of a Si wafer at 977 nm wavelength as a function of incident angle.

That is, the incident light has its electric field normal to the plane of incidence. From Snell's law, the angle of transmitting light is

$$\theta_t = \sin^{-1}\left(\frac{n_i}{n_t} \sin \theta_i\right) = 11.46^\circ.$$

As shown in figure B-4, the reflectance is 44 % for the 977 nm wavelength at an incident angle of 45°. As discussed above, more than 99.9 % of the transmitted light is absorbed within the wafer. Therefore, the fraction of the laser power absorbed by the wafer, η_{Si} , is 0.56.

The total efficiency in laser beam irradiation is obtained by multiplying the efficiency of optical component,

$$\begin{aligned} \varepsilon &= \eta_c \cdot \eta_w \cdot \eta_l \cdot \eta_{Si} \\ &= 0.95 \times 0.90 \times 0.89 \times 0.56 = 0.43 \end{aligned}$$

This value is somewhat smaller than the experimentally obtained value, 0.35. The smaller value can be attributed to the smaller numerical aperture (NA) of the collimator, which causes a loss when collecting the outer boundaries of the laser beam.

Bibliography

- [1] S. Wolf and R. N. Tauber, "Silicon Processing for the VLSI Era, vol.1-Process Technology," Lattice Press, Sunset Beach, CA, 1986
- [2] D. J. Elliott, "Integrated Circuit Fabrication Technology," McGraw-Hill Publ., New York, 1989, p275
- [3] W. Waldo, "Techniques and Tools for Optical Lithography," ed. W. B. Glendinning and J. N. Helbert, Noyes Publ., Park Ridge, NJ, 1991, p353
- [4] W. B. Glendinning and J. N. Helbert, "Handbook of VLSI Microlithography, Principles, Technology and Applications," Noyes Publ., Park Ridge, NJ, 1991, pvii
- [5] L. R. Harriot, Applied Surface Science, 36, 432 (1982)
- [6] S. Namba, Nucl. Instr. and Methods in Physics Research, B39, 504 (1989)
- [7] J. J. Muray, "Physics of Ion Beam Wafer Processing," Semiconductor Int'l., April '84, p130
- [8] I. Brodie and J. M. Muray, "The Physics of Microfabrication," Plenum Press, New York, 1982, p135
- [9] G. Benassayag and P. Sudraud, J. Phys. (Paris) Suppl. No. 12, 45, C9-223 (1984)
- [10] R. Gomer, Appl. Phys. 19, 365 (1979)
- [11] J. Melngailis, J. Vac. Sci. Technol., B5, 469 (1987)
- [12] L. W. Swanson, "Electron Optical Systems for Microscopy Microanalysis and Microlithography," ed. J. Hren, F. Lenz, E. Munro, and P. Sewell, SEM Inc., AMF O'Hare, Chicago, IL, 1984, p135
- [13] K. D. Cummings, L. R. Harriot, G. C. Chi, and F. W. Ostermayer, Jr., SPIE 632, 93 (1986)
- [14] S. K. Ghandhi, "VLSI Fabrication Principles," John Wiley & Sons, New York, 1983
- [15] N. W. Parker, W. P. Robinson, and J. M. Snyder, SPIE, 632, 76 (1986)
- [16] M. Yamamoto, M. Sato, H. Kyogoku, K. Aita, Y. Nakagawa, A. Yasaka, R. Takasawa, and O. Hattori, SPIE, 632, 97 (1986)
- [17] J. Melngailis and P. G. Blauner, Materials Research Society Symposium (San Diego, CA, 1989), 147, 127
- [18] J. Melngailis, SPIE, 1465, p36 (1991)
- [19] A. D. Della Ratta, "Focused Ion Beam Induced Deposition of Copper," Master's Thesis, MIT (1993)
- [20] A. Dubner, A. Wagner, J. Melngailis, and C. V. Thompson, J. Appl. Phys., 70, 665 (1991)
- [21] J. P. Biersack and L. G. Hagmark, Nucl. Instr. and Methods, 174, 257 (1980)
- [22] L. R. Harriot and J. Vasile, J. Vac. Sci. Technol., 36, 1037 (1988)
- [23] Z. Xu, T. Kosugi, K. Gamo, and S. Namba, J. Vac. Sci. Technol. B7, 1959 (1989)
- [24] K. Gamo and S. Namba, Proc. 1989 Int'l Symp. on MicroProcess Conf. p293
- [25] D. K. Stewart, L. A. Stern, and J. C. Morgan, SPIE (1989)
- [26] Y. Madokoro, T. Ohnishi, and T. Ishitani, Riken Conf., Mar. (1989)
- [27] P. G. Blauner, J. S. Ro, Y. Butt, and J. Melngailis, J. Vac. Sci. Technol., B7, 609 (1989)
- [28] P. G. Blauner, Y. Butt, J. S. Ro, C. V. Thompson, and J. Melngailis, J. Vac. Sci. Technol., B7, 1816 (1989)
- [29] T. Tao, J. Ro, J. Melngailis, Z. Xue, and H. D. Kaesz, J. Vac. Sci. Technol., B8, 1826 (1990)
- [30] M. E. Gross, L. R. Harriot, and R. L. Opila, J. Appl. Phys., 68, 4820, (1990)
- [31] H. Komano, Y. Ogata, and T. Takagi, Jpn. J. Appl. Phys., 28, 2372 (1989)

- [32] Y. Takahashi, Y. Madokoro, and T. Ishitani, *Jpn. J. Appl. Phys.*, **30**, 3232 (1991)
- [33] "FIB 500D Operation Manual," FEI Company, Beaverton, OR, 1991
- [34] J. N. Walpole, E. S. Kintzer, S. R. Chinn, C. A. Wang, and L. J. Missaggia, *Appl. Phys. Lett.*, **61**, 740 (1992)
- [35] C. A. Wang and H. K. Choi, *IEEE J. Quantum Electron.*, **27**, 681 (1991)
- [36] J. Walpole and L. Missaggia, Private communication
- [37] H. C. Casey, Jr. and M. B. Panish, "Heterostructure Lasers," Academic Press, New York, 1978, p20
- [38] W. W. Duley, "Laser Processing and Analysis of Materials," Plenum Press, New York, 1983, p1
- [39] J. A. T. Norman, B. A. Muratore, P. N. Dyer, D. A. Roberts, and A. K. Hochberg, *J. De Physique IV*, c2-227 (1991)
- [40] J. A. T. Norman, B. A. Muratore, P. N. Dyer, D. A. Roberts, A. K. Hochberg, and L. H. Dubois, Presented at E-MRS Meeting, Strasbourg, France, June 1992
- [41] J. Han, "Combined Experimental and Modelling Studies of Laser Assisted Chemical Vapor Deposition of Copper and Aluminum," Ph. D. Thesis, MIT (1993)
- [42] A. D. Dubner, "Mechanism of Ion Beam Induced Deposition," Ph. D. Thesis, MIT (1990)
- [45] K. Brugger, *J. Appl. Phys.*, **43**, 577 (1972)
- [46] W. W. Duley, "CO₂ Lasers: Effects and Applications," Academic Press, New York, 1976, p128
- [47] E. Hecht and A. Zajac, "Optics," Addison-Wesley Publ., Reading, MA, 1974
- [48] "Newport Catalog of Precision Laser and Optics Products," Newport Co., Fountain Valley, CA, 1989, pN-28
- [49] H. R. Philip and E. A. Taft, *Phys. Rev.*, **120**, 37 (1962)